Improved One-Way Reflection Waveform Inversion and Strategies for Optimal Offset Selection

Abolhassani, Siamak; Verschuur, Dirk Jacob

DOI
10.1111/1365-2478.70062

Publication date
2025

Document Version
Final published version

Published in
Geophysical Prospecting

Citation (APA)
Abolhassani, S., & Verschuur, D. J. (2025). Improved One-Way Reflection Waveform Inversion and Strategies for Optimal Offset Selection. *Geophysical Prospecting*, *73*(7), Article e70062. https://doi.org/10.1111/1365-2478.70062

Geophysical Prospecting

Geophysical Prospecting

ORIGINAL ARTICLE OPEN ACCESS

Improved One-Way Reflection Waveform Inversion and Strategies for Optimal Offset Selection

Siamak Abolhassani | Dirk Jacob Verschuur

Computational Imaging Laboratory, Department of Imaging Physics, Faculty of Applied Sciences, Delft University of Technology, Delft, The Netherlands

Correspondence: Siamak Abolhassani (s.abolhassani@tudelft.nl)

Received: 11 April 2025 | **Accepted:** 22 July 2025

Funding: The study was supported by the sponsors of the Delphi Consortium.

Keywords: acoustics | full waveform | imaging | inversion | tomography | seismics

ABSTRACT

Conventional reflection waveform inversion solves a two-parameter seismic inverse problem alternately for subsurface reflectivity and acoustic background velocity as the model parameters. It seeks to reconstruct a low-wavenumber velocity model of the subsurface from pure reflection data cyclically, through alternating migration and tomography loops, such that the remodelled data fits the observed data. Low-resolution seismic images with unpreserved amplitudes, full-wave inconsistency in the short-offset data and cycle skipping in the long-offset are perceived as the main reasons for suboptimal tomographic updates and slow convergence in conventional reflection waveform inversion. In the context of one-way reflection waveform inversion, this paper addresses the listed limitations through four main components. First, it augments one-way reflection waveform inversion with a computationally affordable preconditioned least-squares wave equation migration algorithm to ensure high-resolution reflectors with preserved amplitudes. Second, the paper verifies how well the full-wave consistency condition in the short-offset data is satisfied in one-way reflection waveform inversion and suggests muting inconsistent short-offset residual waveforms in the tomography loop to attenuate their adverse imprint. Third, the paper suggests extending the migration offset beyond short offsets to improve both the illumination and the signal-to-noise ratio of the reflectors. Fourth, the paper presents a data-selection algorithm to exclude the damaging effect of the cycle-skipped long-offset data in the tomography loop. The effectiveness of the proposed one-way reflection waveform inversion algorithm is finally validated through three numerical examples, demonstrating its capability to recover high-fidelity tomograms.

1 | Introduction

Since the early 1980s, multiple efforts have been made by geoscientists to recover high-resolution subsurface models (e.g., velocity, density) by explaining observed seismic waveforms. In a big step forward, Tarantola (1984) introduced full waveform inversion (FWI) in the acoustic approximation. Conventional FWI solves a minimization problem by defining an L2-norm misfit function that measures the difference between the modelled and observed seismic waveforms to reconstruct high-resolution subsurface models. While conventional FWI has shown great success in reconstructing high-fidelity shallow subsurface models described by the field data (e.g., Vigh et al. 2011; Liu et al. 2012; Plessix et al. 2013), it has been shown incapable of retrieving deep subsurface targets, where refracted and diving waves do not reach due to the limited offset range in the acquired data (e.g., Irabor and Warner 2016; Vigh et al. 2016; Jones 2019; Brittan and Jones 2019). Given the technical barriers of acquiring ultra-long-offset seismic data, the expenses of modern seismic data acquisition equipment for acquiring long offsets,

physical obstacles in acquisition areas, and short-offset legacy data, conventional FWI cannot always provide the optimum outcome.

While observed refracted and diving waves suffer from limited penetration depth for a given offset, the reflected waves can penetrate deeper. To benefit from pure reflection data and illuminate deep targets, Mora (1989) elaborated on the significance of scale separation, separating the retrieval of high local model wavenumbers (migration process, also called imaging) from the retrieval of low local model wavenumbers (tomography process). After Mora (1989), multiple variations of migration-based velocity analysis (MVA) relying on model-scale separation have been developed. Notably, among these variants, those incorporating wave equation forward modelling have emerged as significant due to their enhanced handling of wave propagation in complex geological environments. Specifically, wave equation MVA (WEMVA) algorithms, as introduced by Sava and Biondi (2004), typically aim to optimize an image-domain error function computed from common image gathers (CIGs). This optimization is achieved using either the classical semblance or a differential semblance (DS) function, which evaluates the flatness or coherency of the CIGs (Chauris and Noble 2001; Shen et al. 2003). WEMVA can also be expressed within the extended-image framework, as described by Shen (2005). Shen and Symes (2008) demonstrated the use of the DS function in conjunction with subsurface-offset CIGs. This approach has been widely studied, and various challenges have been identified and partly addressed – such as the imprint of small-scale heterogeneities on the macromodel update, the need for efficient quantitative migration methods and the limitations arising from incorrect physics, for instance, the constant-density acoustic approximation (see Chauris and Farshad 2023 for a review). Later, Symes (2008) developed a joint framework that combines WEMVA and FWI, known as tomographic full-waveform inversion (TFWI). TFWI has since been further explored by Almomin and Biondi (2012) and D. Sun and Symes (2013), with some practical success, albeit at high computational cost due to the extended-domain imaging condition and the large number of Green's functions involved.

In the meantime and with the same understanding as WEMVA, several reflection waveform inversion (RWI) techniques also originated by combining wave equation migration and FWI into a single framework (e.g., Xu, Wang, Chen, Lambaré, et al. 2012; H. Zhou et al. 2012). RWI, like WEMVA, relies on the idea of model-scale separation; however, such a separation between the migration and tomography sensitivity kernels in waveform inversion has always been challenging. So far, there are three main alternatives to address the challenge: (a) scattering-angle filtering (e.g., Alkhalifah 2014; Xie 2015; Kazei et al. 2016; Wu and Alkhalifah 2017; Yao et al. 2018; Yao, da Silva, Kazei et al. 2019), (b) wavefield decomposition (e.g., Liu et al. 2011; F. Wang et al. 2013; Tang et al. 2013; Irabor and Warner 2016; Chi et al. 2017; Lian et al. 2018), and (c) Born modelling (e.g., Xu, Wang, Chen, Lambaré, et al. 2012; Xu, Wang, Chen, Zhang, et al. 2012; H. Zhou et al. 2012; D. Sun et al. 2016; Vigh et al. 2016; P. Wang et al. 2018). To improve the RWI gradient, some studies examined merging early-arrival waveform inversion and RWI (W. Zhou et al. 2015; Z. Wu and Alkhalifah 2015).

Berkhout (2012; 2014b) introduced an algorithm for reflection waveform inversion – based on wavefield decomposition into upgoing and downgoing waves – and named it joint migration inversion (JMI). Wavefield decomposition in JMI relies on a one-way acoustic wavefield extrapolation scheme known as full wavefield modelling (FWMod) (Berkhout 2014a), which includes both primaries and controlled-order multiples (Verschuur et al. 2016). Angle-independent FWMod is set up on two classes of parameters: acoustic background velocity and angle-independent reflectivity. Due to the adequate parameterization in FWMod, the tomographic and imaging sensitivity kernels in JMI appear independent. Recently, Lu et al. (2018), Dong et al. (2018), Romahn et al. (2021), Hassine et al. (2022) and Soubaras et al. (2023) have also utilized the one-way acoustic wave equation for the purpose of wave equation migration and reflection waveform inversion. Constraining FWMod to single-scattered waveforms-primary wavefield modelling, in short PWMod – we use the same notion as JMI for reflection waveform inversion here and refer to it as one-way reflection waveform inversion (ORWI). As an inverse problem, ORWI alternately solves a two-parameter minimization problem with a misfit function that measures the reflection data (primaries) error in the least-squares sense. Both classes of parameters in ORWI – background velocity and angle-independent reflectivity – are reconstructed in a cyclic process, including least-squares migration and reflection tomography loops (Algorithm 1). Based on a zero initial reflectivity model, a smooth initial background velocity model, and full-offset reflection data in both migration and tomography loops, the flow begins with the migration loop and proceeds to alternate between the loops until reaching convergence with accurate solutions for the background velocity and reflectivity.

Similarly to the process of optimizing a DS function (Chauris and Farshad 2023), building true amplitude and high-resolution reflectors can considerably help any RWI technique recover strong and in-phase tomographic wavepaths in each cycle (Gomes and Yang 2018; Y. Chen et al. 2020). However, iterative least-squares migration (LSM) techniques, for example, least-squares reverse time migration and least-squares one-way wave equation migration, are often expensive to employ in RWI because LSM requires iterations to be converged optimally. Although the number of iterations can be cut down by preconditioning the gradient direction with the reciprocal of the Hessian information, the Hessian computation turns prohibitively costly when dealing with large-scale seismic problems (Lines and Treitel 1984). For cost reduction, Beydoun and Mendes (1989), Chavent and Plessix (1999), Shin et al. (2001) and Plessix and Mulder (2004) approximated the diagonal coefficients of the Hessian matrix rather than full coefficients, and others have tried to approximate the complete coefficients at an affordable cost in either the data or image domain. Pratt et al. (1998) calculated the Gauss–Newton approximation of the Hessian matrix (also known as the linear or approximate Hessian). Hu et al. (2001), Guitton (2004) and Yu et al. (2006) approximated the inverse Hessian by constructing deconvolution filters in the image domain. For a target-oriented imaging problem, explicit computation of a sparse Hessian matrix via cross-correlation of the source and receiver Green's functions is feasible (Valenciano et al. 2006). Choi et al. (2008) replaced the Hessian with a scaled pseudo-Hessian. Point spread functions have also been used to reduce the relevant

ALGORITHM 1 | Cyclic workflow of one-way reflection waveform inversion

```
Providing a smooth initial background velocity and zero initial reflectivity model when cycle number k = 1.
while convergence not reached do
    for i ← 1 to m do
        UPDATE the reflectivity model using one-way wave-equation while keeping the background
        velocity model fixed (migration).
    for j ← 1 to n do
        UPDATE the background velocity model using one-way wave-equation while keeping the
        reflectivity model fixed (reflection tomography).
    k = k + 1   // The reflectivity model (image) can be reset to zero at this point.
```

cost via computing local Hessian matrices in the image domain (Lecomte 2008; Fletcher et al. 2016). The truncated-Newton method is also used to implicitly approximate the application of the inverse Hessian on the gradient vector (Métivier et al. 2013; Assis and Schleicher 2021; Assis et al. 2024). Recently, researchers have also proposed explicit inverse formulas for the one-/two-way modelling operators in the high-frequency limit, mostly compensating for geometrical spreading. In this context, Zhang et al. (2007) and Kiyashchenko et al. (2007) proposed true-amplitude wave equation migration schemes with one-way forward modelling operators. ten Kroode (2012) derived an explicit inversion expression for the Kirchhoff modelling operator, while ten Kroode (2014) and Hou and Symes (2015) derived similar inversion expressions for the Born modelling operator, both in the subsurface-extended domain. In a similar vein to Hou and Symes (2015), Chauris and Cocher (2017) approximated a pseudo-inverse operator for the subsurface-extended Born modelling operator; Chauris and Cocher (2018) presented a comparison of the two methods. A pseudo-inverse operator can also be used as a preconditioner in a gradient-descent inversion scheme to speed up convergence, as demonstrated by Hou and Symes (2016) and Qin and Lambaré (2016). In this paper, to build the approximate Hessian information with affordable computational cost, we use the efficient preconditioned least-squares wave equation migration (PLS-WEM) algorithm recently introduced by Abolhassani and Verschuur (2024). PLS-WEM constructs the approximate Hessian operator recursively, depth by depth, thanks to PWMod. It decomposes and reduces the massive approximate Hessian operator for the entire domain into sub-operators relevant to each depth level. PLS-WEM can recover reflectors to be fit for our purpose in one to five iterations at best.

It is well understood that two-way traveltime varies with both reflector's depth and background velocity, a fundamental problem known as ambiguity in the depth–velocity determination problems. From a traveltime perspective, RWI also aims to resolve this ambiguity and estimate the subsurface model by measuring how much of the overall traveltime error in the reflection data is due to errors in depth versus errors in background velocity. In RWI, the background velocity and reflectivity models are updated alternately. The reflectivity model is obtained by a depth migration, which is expected to fit the kinematics of the short-offset data, while the tomography loop updates the background velocity model based on this reflectivity model. The alternating approach of conventional RWI ignores the fact that a change in the velocity model immediately changes the reflectivity model – by fixing the reflectors' positions in depth while updating the background velocity (Xu, Wang, Chen, Lambaré, et al. 2012; H. Zhou et al. 2012). This results in depth inconsistency between the background velocity and reflectivity models, an issue known as reflectivity–velocity coupling in RWI (Baina and Valensi 2018; Audebert and Cocher 2020; Valensi and Baina 2021; Provenzano et al. 2023). To address this, a first approach has been proposed with pseudo-time domain RWI, where reflectors' positions are calculated in vertical time and are less dependent on background velocity (e.g., Qu et al. 2020; Provenzano et al. 2023), while Valensi and Baina (2021) proposed to take into account the reflectivity–velocity coupling in the RWI tomographic gradient. Note also that the so-called migration-based traveltime tomography (Clément 1991; Chavent et al. 1994) – an idea that somehow inspired the development of RWI itself – had already solved this issue by introducing a reflectivity in the data domain rather than in the image domain. A second issue in RWI is that the reflectivity model obtained after the depth migration loop may not allow for a perfect match of the amplitude and phase of the short-offset data in the tomography loop. This is particularly true when non-short-offset traces are migrated with an erroneous background velocity model, or even when the background velocity is correct but the depth migration is not quantitative in amplitude and phase. This mismatch introduces a full-wave inconsistency between the modelled and observed data in the tomography loop, particularly at short offsets, resulting in an adverse imprint on the tomographic gradient. To address this, several approaches have been suggested so far. Many have attempted to reduce this effect using quantitative migration with short-offset data or even near-zero offset data (W. Zhou et al. 2015; Guo and Alkhalifah 2017; P. Wang et al. 2018; Li et al. 2019; Yao et al. 2020; Hassine et al. 2022; Robin et al. 2023). In another interesting approach, Liang et al. (2022) proposed replacing the conventional image in RWI with an image extracted from stacked, flattened common image gathers. This effect is hereafter referred to as the full-wave inconsistency in the short-offset data. This paper first investigates how effectively the full-wave consistency condition holds between the short-offset modelled and observed data within the context of ORWI. Then, considering that the negative impact of full-wave inconsistency is stronger on the contribution of short offsets in background velocity estimation, we suggest muting short-offset data with inconsistent waveforms in the residual data domain during the tomography loop. Relying on this muting approach, this paper also proposes extending the migration offset beyond near-zero or short offsets to avoid limitations in the reflectors' illumination and amplitudes. This strategy does not match the amplitude and phase of short-offset data but excludes their contribution

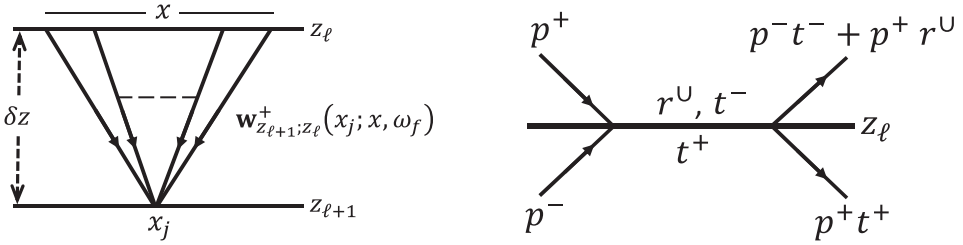

FIGURE 1 | (a) Schematic representation of the jth row of the downward extrapolation matrix $\mathbf{W}^+_{z_{\ell+1};z_\ell}$ for a virtual layer bounded between two virtual depth levels. (b) Schematic representation of how the incident wavefields interact (reflection and transmission) at a particular virtual depth level in PWMod, where $r^\cup$ represents an upward reflection scalar, t^+ represents a downward transmission scalar and t^- represents an upward transmission scalar.

from the tomographic gradient of ORWI (limits their negative impact) and improves illumination and signal-to-noise ratio through an extended migration offset. We define the extended migration offset as the offset at which the misfit function no longer significantly decreases and refer to it as MEMO, which stands for maximum effective migration offset. Note that this paper deals only with the issue of full-wave inconsistency, leaving reflectivity–velocity coupling outside its scope.

Cycle skipping (Virieux and Operto 2009) in long-offset data due to a poor initial background velocity model is perceived as another hurdle in RWI. Building a kinematic-accurate initial background velocity model, multi-scaling (Bunks et al. 1995; Pratt et al. 1998) and adopting alternative misfit functions rather than traditional waveform-based misfit functions have been the most common solutions. Notable among the alternative misfit functions are traveltime-based misfit functions (Luo and Schuster 1991; de Hoop and van Der Hilst 2005; van Leeuwen and Mulder 2010; Ma and Hale 2013; Luo et al. 2016), unwrapped-phase misfit functions (Choi and Alkhalifah 2013, 2014; Choi et al. 2015), envelope-based misfit functions (Bozdağ et al. 2011; R. Wu et al. 2014; Chi et al. 2014; G.-X. Chen et al. 2018), optimal-transport-based misfit functions (Métivier et al. 2016; Yang and Engquist 2018) and the normalized integration method (Chauris et al. 2012; Donno et al. 2013). In this paper, we first illustrate the detrimental contribution of cycle-skipped long-offset data on the tomographic gradient of ORWI. We then introduce, inspired by van Leeuwen and Mulder (2010), a time-domain two-step data-selection algorithm excluding the contribution of the cycle-skipped long-offset residual data in each iteration of the tomography loop to obtain a high-fidelity tomographic update. The algorithm relies on global and local cross-correlations between the observed and modelled reflection data in the time domain.

This paper is organized as follows: After the introduction, we first review the theoretical features of ORWI and reintroduce the PLS-WEM technology to replace the migration core of ORWI. Next, we examine how far the full-wave consistency condition is supported in the context of ORWI. Following this, we describe our approach to mitigating the imprint of full-wave inconsistency on background velocity estimation in ORWI. We then introduce the concept of MEMO and its significance. We also present a workflow to extract the uncycle-skipped part of the long-offset reflection data in each tomography loop. We evaluate our proposal through three numerical examples: two dipping layers placed in a linear background velocity model, the flat section of the Marmousi model and the faulted section of the Marmousi model. We end with a discussion and conclusions.

2 | Standard One-Way Reflection Waveform Inversion

One-way reflection waveform inversion (ORWI) is an acoustic reflection waveform tomography tool based on wavefield decomposition into upgoing and downgoing waves. Wavefield decomposition in ORWI relies on a one-way wavefield extrapolation scheme known as PWMod (Berkhout 2014a), based on first-order scattering and incorporating transmission effects. PWMod perceives wave propagation as a one-way extrapolation from multiple points at z_ℓ to a point at $z_{\ell+1}$, where z_ℓ and $z_{\ell+1}$ denote two subsequent virtual depth levels, respectively. The absolute value of the vertical distance between z_ℓ and $z_{\ell+1}$ is called the extrapolation step and is considered small enough to be assumed homogeneous vertically. The upward and downward data extrapolations are performed using extrapolation kernels, which are the analytical solutions to the acoustic wave equation in a homogeneous medium in the frequency-wavenumber domain. PWMod defines the two-dimensional forward extrapolated wavefield from all lateral positions located at z_ℓ towards a lateral position located at $z_{\ell+1}$ in the $+z$ direction as a frequency-space convolution integral along the x-axis (Rayleigh integral II in two dimensions)

$$p^+(x_j, z_{\ell+1}, \omega_f) = \int_{-\infty}^{+\infty} p^+(x, z_\ell, \omega_f) w^+_{z_{\ell+1};z_\ell}(x_j; x_j - x, \omega_f) dx, \tag{1}$$

in which $w^+_{z_{\ell+1};z_\ell}$ denotes the monochromatic downward wavefield extrapolation kernel from the virtual depth level z_ℓ to one lateral position at the virtual depth level $z_{\ell+1}$, the index j means the lateral position at $z_{\ell+1}$, x_j is the convolution lag, ω_f is a given angular frequency, $p^+(x, z_\ell, \omega_f)$ is the monochromatic downgoing wavefield located at z_ℓ and $p^+(x_j, z_{\ell+1}, \omega_f)$ is the monochromatic downgoing wavefield at the lateral position x_j located at $z_{\ell+1}$. The wavefield extrapolation kernel in Equation (1) reads

$$w^+_{z_{\ell+1};z_\ell}(x_j; x_o, \omega_f) = \frac{1}{2\pi} \int_{-\infty}^{+\infty} \mathrm{e}^{-i\sqrt{\left(\frac{\omega_f}{v_j}\right)^2 - k_x^2}|\delta z|} \mathrm{e}^{-ik_x x_o} dk_x, \tag{2}$$

in which the integral represents the inverse Fourier transform of the downward extrapolation kernel-downward phase-shift extrapolation kernel-in the frequency-wavenumber domain in the x-direction, the index o means the lateral position at $z_\ell, x_j; x_o$ means from x_o to x_j, δz represents the extrapolation step and equals the vertical distance between z_ℓ and $z_{\ell+1}$, v_j represents the velocity value at x_j between the virtual depth levels z_ℓ and $z_{\ell+1}$ and k_x is the horizontal wavenumber.

The downward extrapolation kernel in its matrix form is expressed as

$$\mathbf{W}^{+}_{z_{\ell+1};z_\ell} = \begin{bmatrix} \mathbf{w}^{+}_{z_{\ell+1};z_\ell}\left(x_1; x, \omega_f\right) & & & \\ & \ddots & & \\ & & \mathbf{w}^{+}_{z_{\ell+1};z_\ell}\left(x_j; x, \omega_f\right) & \\ & & & \ddots \\ & & & \mathbf{w}^{+}_{z_{\ell+1};z_\ell}\left(x_{n_x}; x, \omega_f\right) \end{bmatrix}, \quad (3)$$

where n_x shows the total number of model parameters located on each virtual depth level, $\mathbf{W}^{+}_{z_{\ell+1};z_\ell}$ is a square matrix of dimension $n_x \times n_x$ and $\mathbf{w}^{+}_{z_{\ell+1};z_\ell}\left(x_j; x, \omega_f\right)$ represents a row vector. For a virtual layer without lateral velocity variations, $\mathbf{W}^{+}_{z_{\ell+1};z_\ell}$ becomes a Toeplitz matrix (Berkhout 1982, 164), and for a laterally inhomogeneous virtual layer, defined by locally averaged velocities, $\mathbf{W}^{+}_{z_{\ell+1};z_\ell}$ becomes a space-variant convolutional matrix (Thorbecke et al. 2004). Figure 1a schematically displays one row of $\mathbf{W}^{+}_{z_{\ell+1};z_\ell}$. If more clarification is required, the extrapolation kernel is further described in Berkhout (2014a).

PWMod reads the following equations – in the vector–matrix form-to model the angle-independent primary reflection data (traditional surface seismic data excluding direct waves, refractions, and diving waves), including reflection and transmission effects (Figure 1b)

$$\mathbf{p}^{-}_{\mathrm{mod}}\left(z_0, \omega_f\right) = \sum_{m=N}^{1}\left[\left[\prod_{n=1}^{m-1}\mathbf{W}^{-}_{z_{n-1};z_n}\mathbf{T}^{-}(z_n)\right]\mathbf{W}^{-}_{z_{m-1};z_m}\right]\left(\mathbf{r}^{\cup}(z_m)\circ\mathbf{p}^{+}_{\mathrm{mod}}\left(z_m, \omega_f\right)\right), \quad (4)$$

$$\mathbf{p}^{+}_{\mathrm{mod}}\left(z_m, \omega_f\right) = \left[\left[\prod_{n=m-1}^{1}\mathbf{W}^{+}_{z_{n+1};z_n}\mathbf{T}^{+}(z_n)\right]\mathbf{W}^{+}_{z_1;z_0}\right]\mathbf{s}^{+}\left(z_0, \omega_f\right), \quad (5)$$

in which $\mathbf{p}^{-}_{\mathrm{mod}}\left(z_0, \omega_f\right)$ is the monochromatic upgoing wavefield modelled at z_0 and $\mathbf{p}^{+}_{\mathrm{mod}}\left(z_m, \omega_f\right)$ is the monochromatic downgoing wavefield modelled at z_m. The matrix–matrix multiplication operations enclosed by the outer square brackets in Equation (4) contain the upward extrapolation operator ($\mathbf{W}^{-}$) along with the upward transmission diagonal-matrix-operator ($\mathbf{T}^{-}(z_n) = \mathbf{I} - \mathrm{diag}(\mathbf{r}^{\cup}(z_n))$, encapsulating all the operators required for a wavefield to reach from z_m to z_0. The matrix–matrix multiplication operations enclosed by the outer square brackets in Equation (5) contain the downward extrapolation operator ($\mathbf{W}^{+}$) along with the downward transmission diagonal-matrix-operator ($\mathbf{T}^{+}(z_n) = \mathbf{I} + \mathrm{diag}(\mathbf{r}^{\cup}(z_n))$, encapsulating all the operators required for a wavefield to reach from z_0 to z_m. Here, $\mathbf{r}^{\cup}(z_m)$ represents the angle-independent upward reflectivity vector-operator at z_m, $\mathbf{s}^{+}\left(z_0, \omega_f\right)$ shows the monochromatic downgoing physical source at the Earth's surface, N is the total number of virtual depth levels and the symbol $\circ$ means element-wise product. Note that, diag(.) represents a mathematical function that receives a vector and gives a diagonal matrix as its output, and $\mathbf{I}$ means the identity matrix.

ORWI inverts for reflectivity and background velocity (two different classes of parameters) by minimizing the errors in primary reflection waveforms for each class of parameters alternately. Standard ORWI originally aims to minimize the following two-parameter misfit function iteratively:

$$C = \frac{1}{2}\sum_{f=1}^{N_f}\sum_{s=1}^{N_s}\left\|\mathbf{p}^{-}_{\mathrm{obs},s}\left(z_0, \omega_f\right) - \mathbf{p}^{-}_{\mathrm{mod},s}\left(z_0, \omega_f; \mathbf{r}^{\cup}, \mathbf{v}\right)\right\|_2^2, \quad (6)$$

in which $\mathbf{p}^{-}_{\mathrm{obs},s}\left(z_0, \omega_f\right)$ represents the observed monochromatic multiple-free reflection waveforms for shot s recorded at the receiver locations, $\mathbf{p}^{-}_{\mathrm{mod},s}\left(z_0, \omega_f\right)$ represents the modelled monochromatic primary reflection waveforms for shot s recorded at the receiver locations, the vector difference $\mathbf{p}^{-}_{\mathrm{obs},s}\left(z_0, \omega_f\right) - \mathbf{p}^{-}_{\mathrm{mod},s}\left(z_0, \omega_f\right)$ is called the monochromatic residual data vector for shot s and represented later by $\delta\mathbf{d}^{-}_{s}\left(\omega_f\right)$, $\mathbf{v}$ represents the background velocity vector, $\mathbf{r}^{\cup}$ represents the angle-independent upward reflectivity vector, N_s is the total number of shots and N_f is the total number of angular frequency components.

Taking the partial derivatives of the misfit function with respect to $\mathbf{r}^{\cup}$ and $\mathbf{v}$ gives the total descent direction as

$$\mathbf{g} = \begin{bmatrix} \mathbf{g}^{r}(z_0) \\ \vdots \\ \mathbf{g}^{r}(z_N) \\ \mathbf{g}^{v}(z_0) \\ \vdots \\ \mathbf{g}^{v}(z_N) \end{bmatrix} = -\sum_{f=1}^{N_f}\sum_{s=1}^{N_s}\Re\left\{\overbrace{\left[\overbrace{\frac{\partial\mathbf{p}^{-}_{\mathrm{mod},s}\left(z_0, \omega_f\right)}{\partial\mathbf{r}^{\cup}(z_0)} \cdots \frac{\partial\mathbf{p}^{-}_{\mathrm{mod},s}\left(z_0, \omega_f\right)}{\partial\mathbf{r}^{\cup}(z_N)} \frac{\partial\mathbf{p}^{-}_{\mathrm{mod},s}\left(z_0, \omega_f\right)}{\partial\mathbf{v}(z_0)} \cdots \frac{\partial\mathbf{p}^{-}_{\mathrm{mod},s}\left(z_0, \omega_f\right)}{\partial\mathbf{v}(z_N)}}^{\mathbf{J}_s(\omega_f)}\right]^{\dagger}\delta\mathbf{d}^{-}_{s}\left(\omega_f\right)}^{\mathbf{g}_s(\omega_f)}\right\}, \quad (7)$$

in which $\mathbf{g}$ denotes the total two-parameter gradient vector, $\mathbf{g}^{r}(z_m)$ shows the reflectivity gradient at a given depth level for migration, $\mathbf{g}^{v}(z_m)$ shows the background velocity gradient between z_m and z_{m+1} for tomography (for simplicity, shown in notation at z_m),

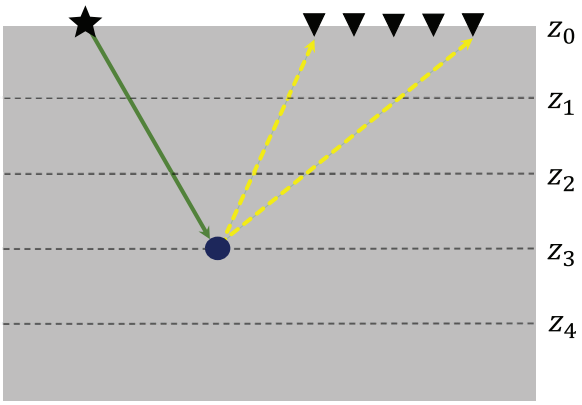

FIGURE 2 | Schematic representation of one element of the reflectivity gradient for one shot, Equation (10), in a medium including five virtual depth levels. Green signifies forward wavefields, while yellow denotes back-propagated wavefields.

$\mathbf{g}_s(\omega_f)$ is the total gradient vector for one shot and one frequency, $\dagger$ means the adjoint operator, $\mathbf{J}_s(\omega_f)$ is the total Jacobian matrix for one shot and one frequency and each column of $\mathbf{J}_s(\omega_f)$ denotes the partial derivative of the upgoing modelled wavefield at the receiver locations with respect to the model parameters of one class, either reflectivity or background velocity, located at a given depth level.

Similarly to RWI (Xu, Wang, Chen, Lambaré, et al. 2012; Xu, Wang, Chen, Zhang, et al. 2012), the two-parameter nature of ORWI – as a minimization problem – is turned into a single-parameter by keeping a class of parameters constant while updating the other class. As a result, Equation (7) is broken into two parts:

$$\mathbf{g}^r = -\sum_{f=1}^{N_f}\sum_{s=1}^{N_s}\Re\left\{\left[\frac{\partial \mathbf{p}^-_{\mathrm{mod},s}(z_0,\omega_f)}{\partial \mathbf{r}^{\cup}(z_0)}\cdots\frac{\partial \mathbf{p}^-_{\mathrm{mod},s}(z_0,\omega_f)}{\partial \mathbf{r}^{\cup}(z_N)}\right]^{\dagger}\delta\mathbf{d}^-_s(\omega_f)\right\}, \tag{8}$$

$$\mathbf{g}^{\upsilon} = -\sum_{f=1}^{N_f}\sum_{s=1}^{N_s}\Re\left\{\left[\frac{\partial \mathbf{p}^-_{\mathrm{mod},s}(z_0,\omega_f)}{\partial \mathbf{v}(z_0)}\cdots\frac{\partial \mathbf{p}^-_{\mathrm{mod},s}(z_0,\omega_f)}{\partial \mathbf{v}(z_N)}\right]^{\dagger}\delta\mathbf{d}^-_s(\omega_f)\right\}, \tag{9}$$

where $\mathbf{g}^r$ shows the total reflectivity gradient for migration and $\mathbf{g}^{\upsilon}$ shows the total velocity gradient for tomography. Indeed, with such a gradient separation, ORWI turns into an iterative cycle alternating between LS-WEM and least-squares one-way wave equation reflection tomography (LS-WET) until the data residual vanishes (Algorithm 1).

Expanding one component of Equation (8), which denotes the reflectivity gradient for a particular depth level, frequency component and shot, yields (Figure 2)

$$\mathbf{g}^r_s(z_m,\omega_f) = -\Re\left\{\left(\mathbf{p}^+_{\mathrm{mod},s}(z_m,\omega_f)\right)^* \circ \overbrace{\left(\mathbf{L}^{-\dagger}_{z_0;z_m}\delta\mathbf{d}^-_s(\omega_f)\right)}^{\text{Back-propagated wavefield}}\right\}, \tag{10}$$

in which $\mathbf{L}^-_{z_0;z_m}$ is defined as

$$\mathbf{L}^-_{z_0;z_m} = \left[\prod_{n=1}^{m-1}\mathbf{W}^-_{z_{n-1};z_n}\mathbf{T}^-(z_n)\right]\mathbf{W}^-_{z_{m-1};z_m}. \tag{11}$$

Expanding one component of Equation (9), which denotes the velocity gradient for a particular depth level, frequency component and shot, yields (Figure 3)

$$\begin{aligned}\mathbf{g}^{\upsilon}_s(z_m,\omega_f) = \mathbf{g}^{\upsilon_A}_s(z_m,\omega_f) + \mathbf{g}^{\upsilon_B}_s(z_m,\omega_f) = &-\Re\left\{\mathbf{G}^{-*}_{z_m;z_{m+1}}\mathbf{q}^{-*}_{\mathrm{mod},s}(z_{m+1},\omega_f)\circ\overbrace{\left(\left(\mathbf{L}^-_{z_0;z_m}\mathbf{T}^-(z_m)\right)^{\dagger}\delta\mathbf{d}^-_s(\omega_f)\right)}^{\text{Back-propagated wavefield}}\right\}\\ &-\Re\left\{\mathbf{G}^{+*}_{z_{m+1};z_m}\mathbf{q}^{+*}_{\mathrm{mod},s}(z_m,\omega_f)\circ\overbrace{\left(\left[\mathbf{L}^-_{z_0;z_{m+1}}\mathbf{R}^{\cup}(z_{m+1})+\left[\sum_{m'=N}^{m+2}\mathbf{L}^-_{z_0;z_{m'}}\mathbf{R}^{\cup}(z_{m'})\mathbf{L}^+_{z_{m'};z_{m+1}}\right]\mathbf{T}^+(z_{m+1})\right]^{\dagger}\delta\mathbf{d}^-_s(\omega_f)\right)}^{\text{Back-propagated wavefield}}\right\},\end{aligned} \tag{12}$$

and given the assumption that $\mathbf{W}^+_{z_{m+1};z_m}$ approximates $\mathbf{W}^-_{z_m;z_{m+1}}$, $\mathbf{G}$ is defined as

$$\mathbf{G}^+_{z_{m+1};z_m} = \mathbf{G}^-_{z_m;z_{m+1}} = \begin{bmatrix}\frac{\partial \mathbf{w}_{1,\star}}{\partial \upsilon_1}\\ \frac{\partial \mathbf{w}_{2,\star}}{\partial \upsilon_2}\\ \vdots\\ \frac{\partial \mathbf{w}_{n_x,\star}}{\partial \upsilon_{n_x}}\end{bmatrix}, \tag{13}$$

in which $\mathbf{w}_{j,\star}$ means the jth row of $\mathbf{W}^-_{z_m;z_{m+1}}$ and

$$\begin{aligned}\mathbf{q}^-_{\mathrm{mod},s}(z_{m+1},\omega_f) &= \mathbf{T}^-(z_{m+1})\,\mathbf{p}^-_{\mathrm{mod},s}(z_{m+1},\omega_f) + \mathbf{R}^{\cup}(z_{m+1})\,\mathbf{p}^+_{\mathrm{mod},s},\\ (z_{m+1},\omega_f)\,\mathbf{q}^+_{\mathrm{mod},s}(z_m,\omega_f) &= \mathbf{T}^+(z_m)\,\mathbf{p}^+_{\mathrm{mod},s}(z_m,\omega_f),\end{aligned} \tag{14}$$

in which $\mathbf{R}^{\cup}(z_{m+1}) = \mathrm{diag}(\mathbf{r}^{\cup}(z_{m+1}))$. It is important to recall that while Equation (12) represents the background velocity gradient at z_m in notation, it updates the background

velocity over the depth interval between z_m and z_{m+1} in practice.

To optimize the update direction, standard ORWI preconditions both gradient vectors as follows (equivalent to equation 27 in Plessix and Mulder (2004))

$$\delta\mathbf{r}^{\cup}(z_m)=\Re\left\{\overbrace{\sum_{f=1}^{N_f}\sum_{s=1}^{N_s}\left(\mathbf{p}^{+}_{\mathrm{mod,s}}\left(z_m,\omega_f\right)\circ\mathbf{p}^{+^*}_{\mathrm{mod,s}}\left(z_m,\omega_f\right)\right)\circ\left(\sum_{g=1}^{N_g}\left[\mathbf{L}^{-}_{z_0;z_m}\right]_{g,\star}\circ\left[\mathbf{L}^{-^*}_{z_0;z_m}\right]_{g,\star}\right)^{T}}^{\text{Preconditioner (a column vector)}}\right\}^{-1}\circ\mathbf{g}^{r}(z_m),\tag{15}$$

and

$$\begin{aligned}\delta\mathbf{v}(z_m)=&\Re\left\{\overbrace{\sum_{f=1}^{N_f}\sum_{s=1}^{N_s}\left(\mathbf{q}^{-}_{\mathrm{mod,s}}\left(z_{m+1},\omega_f\right)\circ\mathbf{q}^{-^*}_{\mathrm{mod,s}}\left(z_{m+1},\omega_f\right)\right)\circ\left(\sum_{g=1}^{N_g}\left[\Theta\right]_{g,\star}\circ\left[\Theta^*\right]_{g,\star}\right)^{T}}^{\text{Preconditioner (a column vector)}}\right\}^{-1}\circ\mathbf{g}^{\upsilon_A}(z_m)\\&+\Re\left\{\overbrace{\sum_{f=1}^{N_f}\sum_{s=1}^{N_s}\left(\mathbf{q}^{+}_{\mathrm{mod,s}}\left(z_m,\omega_f\right)\circ\mathbf{q}^{+^*}_{\mathrm{mod,s}}\left(z_m,\omega_f\right)\right)\circ\left(\sum_{g=1}^{N_g}\left[\Psi\right]_{g,\star}\circ\left[\Psi^*\right]_{g,\star}\right)^{T}}^{\text{Preconditioner (a column vector)}}\right\}^{-1}\circ\mathbf{g}^{\upsilon_B}(z_m),\end{aligned}\tag{16}$$

with

$$\begin{aligned}\Theta&=\mathbf{L}^{-}_{z_0;z_m}\mathbf{T}^{-}(z_m)\mathbf{G}^{-}_{z_m;z_{m+1}},\\\Psi&=\left[\mathbf{L}^{-}_{z_0;z_{m+1}}\mathbf{R}^{\cup}(z_{m+1})+\left[\sum_{m'=N}^{m+2}\mathbf{L}^{-}_{z_0;z_{m'}}\mathbf{R}^{\cup}(z_{m'})\mathbf{L}^{+}_{z_{m'};z_{m+1}}\right]\mathbf{T}^{+}(z_{m+1})\right]\mathbf{G}^{+}_{z_{m+1};z_m},\end{aligned}\tag{17}$$

where $\delta\mathbf{r}^{\cup}(z_m)$ represents the reflectivity update/perturbation vector at z_m and $\delta\mathbf{v}(z_m)$ is the background velocity update/perturbation vector between z_m and z_{m+1}.

Finally, standard ORWI updates the total angle-independent upward reflectivity and background velocity vectors as

$$\mathbf{r}^{\cup}_{k+1}=\mathbf{r}^{\cup}_{k}+\alpha^{r}_{k}\delta\mathbf{r}^{\cup}_{k},\tag{18}$$

$$\mathbf{v}_{k+1}=\mathbf{v}_{k}+\alpha^{\upsilon}_{k}\delta\mathbf{v}_{k},\tag{19}$$

in which k means the current cycle number, $\delta\mathbf{r}^{\cup}$ is the total reflectivity perturbation vector, $\delta\mathbf{v}$ is the total velocity perturbation vector and α^{υ} and α^{r} represent the minimization step lengths for estimating reflectivity and background velocity, respectively. For α^{r}_{k}, we use

$$\alpha^{r}_{k}=\frac{\delta\mathbf{d}^{\dagger}\left(\mathbf{r}^{\cup}_{k}+\delta\mathbf{r}^{\cup}_{k},\mathbf{v}_k\right)\delta\mathbf{d}\left(\mathbf{r}^{\cup}_{k},\mathbf{v}_k\right)}{\delta\mathbf{d}^{\dagger}\left(\mathbf{r}^{\cup}_{k}+\delta\mathbf{r}^{\cup}_{k},\mathbf{v}_k\right)\delta\mathbf{d}\left(\mathbf{r}^{\cup}_{k}+\delta\mathbf{r}^{\cup}_{k},\mathbf{v}_k\right)},\tag{20}$$

and for α^{υ}_{k}, we use

$$\alpha^{\upsilon}_{k}=\frac{\delta\mathbf{d}^{\dagger}\left(\mathbf{r}^{\cup}_{k+1},\mathbf{v}_k+\delta\mathbf{v}_k\right)\delta\mathbf{d}\left(\mathbf{r}^{\cup}_{k+1},\mathbf{v}_k\right)}{\delta\mathbf{d}^{\dagger}\left(\mathbf{r}^{\cup}_{k+1},\mathbf{v}_k+\delta\mathbf{v}_k\right)\delta\mathbf{d}\left(\mathbf{r}^{\cup}_{k+1},\mathbf{v}_k+\delta\mathbf{v}_k\right)},\tag{21}$$

where $\delta\mathbf{d}$ is the superposition of all shots and the frequency components within the range. For more information on the gradient derivation, see Y. Sun et al. (2019).

3 | Enhanced Migration Algorithm in One-Way Reflection Waveform Inversion

In this section, we introduce the first of our four proposed improvements to the one-way reflection waveform inversion (ORWI) methodology, with which we aim to enhance the migration algorithm embedded within ORWI. Least-squares migration (LSM) techniques have proven to be computationally expensive as their convergence requires multiple iterations. Gradient preconditioning helps reduce the number of LSM iterations. The preconditioned least-squares one-way wave equation migration (PLS-WEM) introduced by Abolhassani and Verschuur (2024) is a depth least-squares migration technology that recovers high-resolution and accurate seismic images by reconstructing the approximate Hessian information recursively in depth; PLS-WEM accelerates the convergence of the migration process after employing the reciprocal of the approximate Hessian information for gradient preconditioning. PLS-WEM is relatively fast when compared to similar technologies because it recursively calculates the approximate Hessian operator depth by depth rather than calculating one huge approximate Hessian for the entire medium. This reduces the huge approximate Hessian operator for the entire domain into smaller, depth-dependent operators. Furthermore, as PLS-WEM uses PWMod for forward modelling, this facilitates switching from LS-WEM to PLS-WEM in the

standard ORWI cycle. This section provides an overview of the PLS-WEM theory.

To incorporate gradient preconditioning into Equation (8), PLS-WEM minimizes the misfit function (Shin et al. 2001; Jang et al. 2009; Oh and Min 2013)

$$C = \frac{1}{2}\sum_{f=1}^{N_f}\sum_{s=1}^{N_s}\left\|\delta\mathbf{d}_s^-(\omega_f) - \mathbf{J}_s^r(\omega_f)\delta\mathbf{r}^{\cup}(\omega_f)\right\|_2^2, \tag{22}$$

where $\mathbf{J}_s^r(\omega_f) = \frac{\partial \mathbf{p}^-_{\mathbf{mod},s}(z_0,\omega_f)}{\partial \mathbf{r}^{\cup}}$ and is called the total monochromatic reflectivity Jacobian for shot s.

The stationary point of Equation (22) with respect to $\delta\mathbf{r}^{\cup}(\omega_f)$ is given by

$$\delta\mathbf{r}^{\cup} = -\sum_{f=1}^{N_f}\left(\Re\left\{\sum_{s=1}^{N_s}\mathbf{H}_s^{r,\mathrm{a}}(\omega_f)\right\}^{-1}\Re\left\{\sum_{s=1}^{N_s}\mathbf{g}_s^r(\omega_f)\right\}\right), \tag{23}$$

with $\mathbf{g}_s^r(\omega_f)$ and $\mathbf{H}_s^{r,\mathrm{a}}(\omega_f)$ defined as

$$\mathbf{g}_s^r(\omega_f) = \mathbf{J}_s^{r\dagger}(\omega_f)\delta\mathbf{d}_s^-(\omega_f), \tag{24}$$

$$\mathbf{H}_s^{r,\mathrm{a}}(\omega_f) = \mathbf{J}_s^{r\dagger}(\omega_f)\mathbf{J}_s^r(\omega_f), \tag{25}$$

in which $\mathbf{J}_s^r(\omega_f)$ denotes the monochromatic reflectivity Jacobian for shot s, $\mathbf{g}_s^r(\omega_f)$ represents the monochromatic reflectivity gradient for shot s (mathematically derived in Equation (10) for each virtual depth level), and $\mathbf{H}_s^{r,\mathrm{a}}(\omega_f)$ refers to the monochromatic reflectivity approximate Hessian for shot s compensating for geometrical spreading, spatial correlations of neighbouring model parameters on the same virtual depth levels (Pratt et al. 1998) and also conducting source deconvolution as it acts on the gradient vector frequency by frequency.

Thanks to PWMod, each column of the total monochromatic reflectivity Jacobian for shot s, introduced in Equation (24), satisfies

$$\mathbf{J}_s^r(z_m,\omega_f) = \frac{\partial \mathbf{p}^-_{\mathrm{mod},s}(z_0,\omega_f)}{\partial \mathbf{r}^{\cup}(z_m)}. \tag{26}$$

Abolhassani and Verschuur (2024) showed that $\mathbf{J}_s^r(z_m,\omega_f)$ can be expressed as follows:

$$\mathbf{J}_s^r(z_m,\omega_f) = \left[\prod_{n=m-1}^{1}\mathbf{W}^-_{z_{n-1};z_n}\mathbf{T}^-(z_n)\right]\mathbf{W}^-_{z_{m-1};z_m}$$
$$\left[\begin{pmatrix} p^+_{1\,\mathrm{mod},s}(z_m,\omega_f)\\ 0\\ \vdots\\ 0\end{pmatrix}\begin{pmatrix} 0\\ p^+_{2\,\mathrm{mod},s}(z_m,\omega_f)\\ \vdots\\ 0\end{pmatrix}\cdots\begin{pmatrix} 0\\ 0\\ \vdots\\ p^+_{n_x\,\mathrm{mod},s}(z_m,\omega_f)\end{pmatrix}\right], \tag{27}$$

in which n_x denotes the number of gridpoints at z_m, $p^+_{j\,\mathrm{mod},s}(z_m,\omega_f)$ is the monochromatic downgoing modelled wavefield at the jth gridpoint of z_m and $\mathbf{J}_s^r(z_m,\omega_f)$ is a matrix of dimension $n_x \times n_x$. Plugging Equation (27) into Equation (25) yields $\mathbf{H}_s^{r,\mathrm{a}}(z_m,\omega_f)$. Adopting Equation (23) for each virtual depth level, the reflectivity update vector $\delta\mathbf{r}^{\cup}(z_m)$ is now constructed. Clearly, Equation (23) requires a direct inversion of the approximate Hessian matrix for each frequency component. Finally, Equation (18) is used to update the total angle-independent upward reflectivity vector.

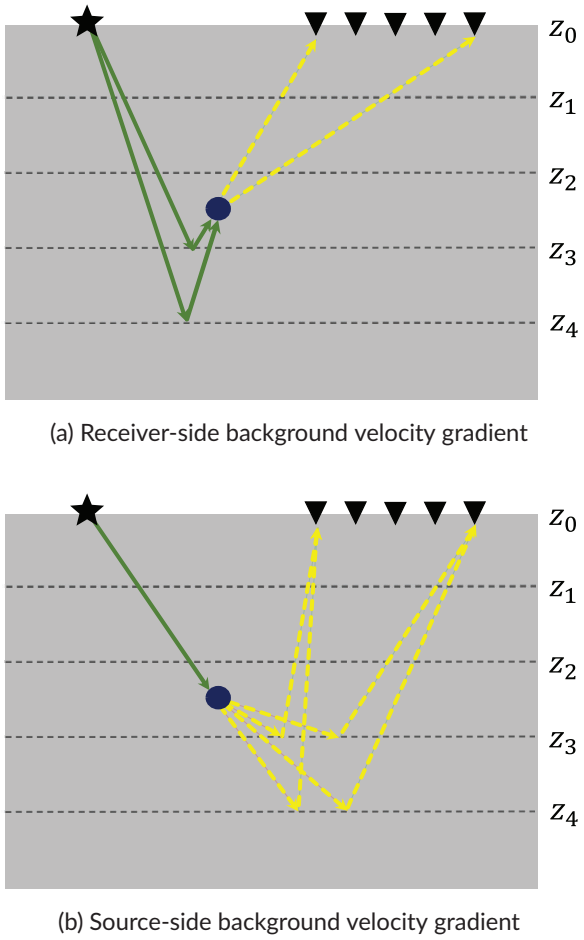

FIGURE 3 | Schematic representation of one element of the background velocity gradient for one shot, Equation (12), in a medium including five virtual depth levels. (a) Receiver-side background velocity gradient for one shot: the term $\mathbf{g}_s^{v_A}(z_m,\omega_f)$ from Equation (12). (b) Source-side background velocity gradient for one shot: the term $\mathbf{g}_s^{v_B}(z_m,\omega_f)$ from Equation (12). Green signifies forward wavefields, while yellow denotes back-propagated wavefields.

PLS-WEM is computationally more feasible compared to alternative technologies that approximate Hessian coefficients at once, as it operates in a depth-marching regime. PLS-WEM achieves this by decomposing and reducing the entire approximate Hessian operator into multiple smaller sub-operators. Each of these sub-operators is relevant to a single virtual depth level and captures only the correlation of the partial derivative wavefields at that depth level. If assembled together for all virtual depth levels, these operators form a block-diagonal presentation of the approximate Hessian operator for the entire medium. With PLS-WEM, each time $\mathbf{H}_s^{r,\mathrm{a}}(z_m,\omega_f)$ and its reciprocal are calculated, indeed, only $1/N$ of the total number of model parameters is involved (Abolhassani and Verschuur 2024).

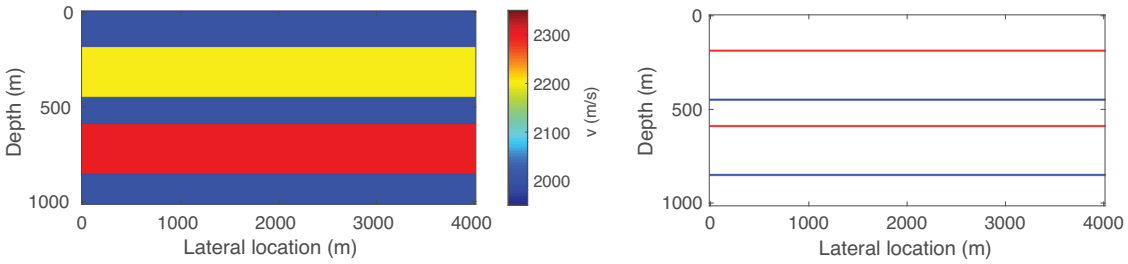

(a) True background velocity model (b) True reflectivity model

FIGURE 4 | Flat-layered medium. (a) True background velocity model. (b) True reflectivity model. In the reflectivity model, red indicates positive reflectivity values (velocity increases with depth), while blue represents negative reflectivity values (velocity decreases with depth).

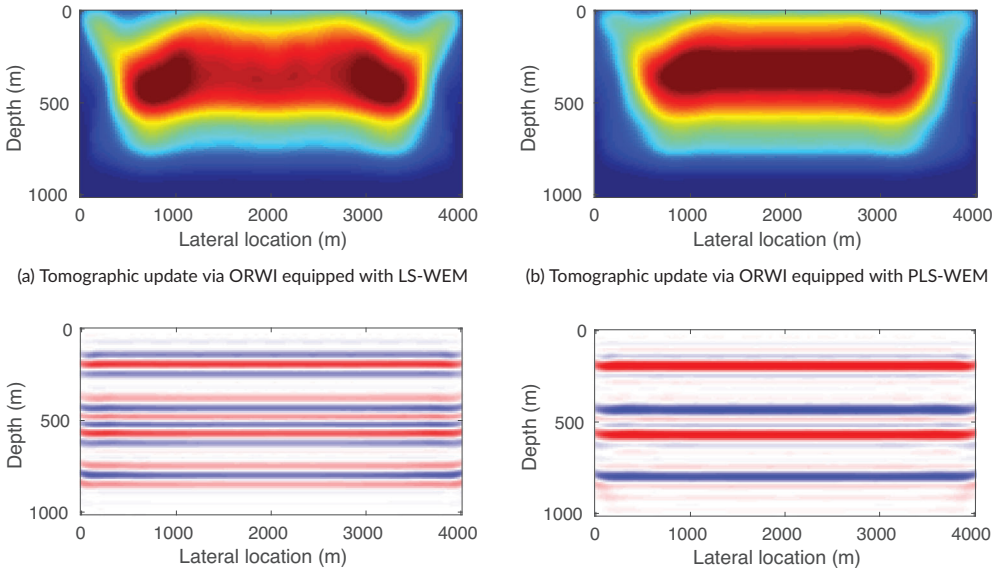

(a) Tomographic update via ORWI equipped with LS-WEM (b) Tomographic update via ORWI equipped with PLS-WEM

(c) Image update with LS-WEM (d) Image update with PLS-WEM

FIGURE 5 | Estimated background velocity models after 1 cycle of ORWI based on LS-WEM and PLS-WEM images, associated with the flat-layered medium shown in Figure 4. (a) and (c) Tomographic and imaging updates after 1 cycle of ORWI equipped with LS-WEM (standard ORWI). (b) and (d) Tomographic and imaging updates after 1 cycle of ORWI equipped with the PLS-WEM image.

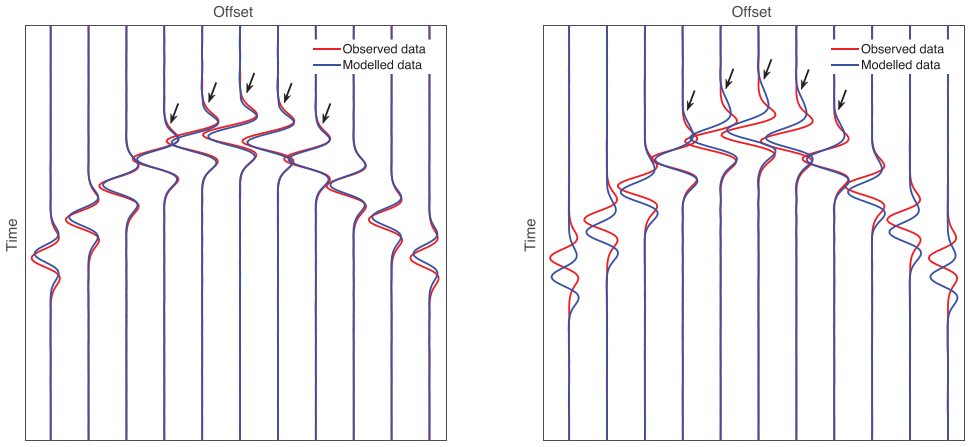

(a) $v_{initial} > v_{true}$ (b) $v_{initial} < v_{true}$

FIGURE 6 | Modelled and observed waveforms for a flat reflector medium with a homogeneous overburden when the full-wave consistency condition is not met at short offsets. (a) The homogeneous initial velocity is greater than the true velocity. (b) The homogeneous initial velocity is less than the true velocity.

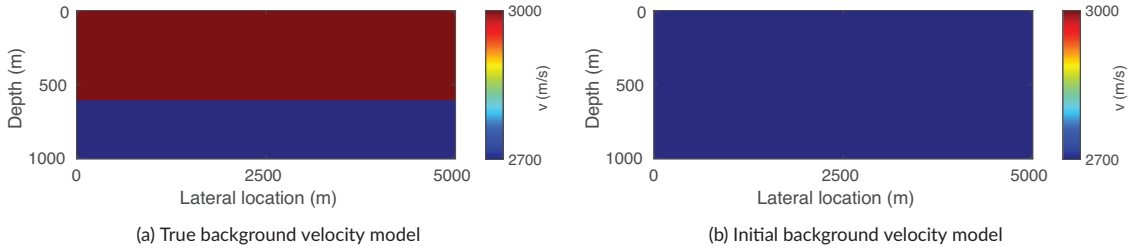

FIGURE 7 | Single-reflector medium. (a) True background velocity model. (b) Initial background velocity model.

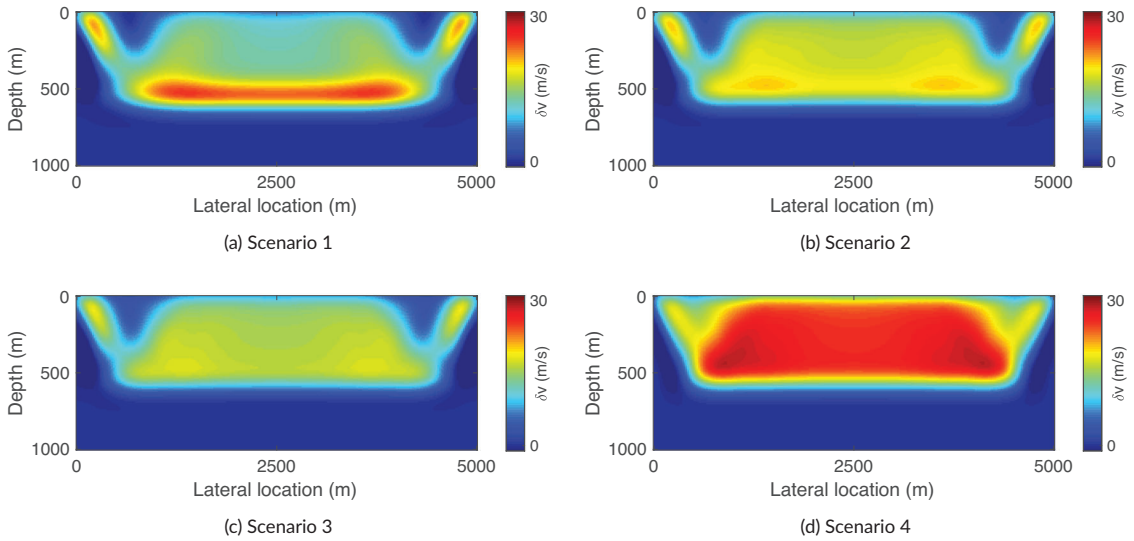

FIGURE 8 | Tomographic updates of ORWI associated with the single-reflector medium after one cycle in four different data scenarios introduced in Table 1. (a) Tomographic update estimated by ORWI when the full offset range is used for both imaging and tomography (Scenario 1). (b) Tomographic update estimated by ORWI after excluding contributions of the cycle-skipped long-offset data to the tomographic gradient – that is, | offset | < 1000 m (Scenario 2). (c) Tomographic update estimated by ORWI after excluding contributions of the cycle-skipped long-offset data to the tomographic gradient and using the same offset range for imaging as for tomography – that is, | offset | < 1000 m (Scenario 3). (d) Tomographic update estimated by ORWI after muting short-offset tomographic wavepaths, coupled with excluding contributions of the cycle-skipped long-offset data to the tomographic gradient, and using the same offset range for imaging as for tomography – that is, | offset | < 1000 m (Scenario 4).

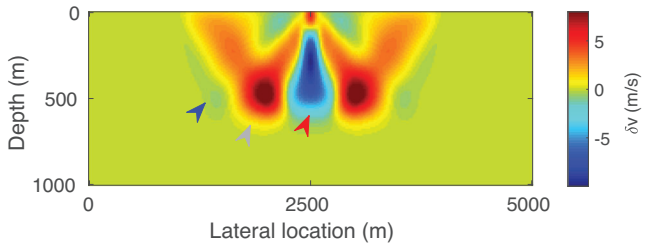

FIGURE 9 | The middle-shot subset of the tomographic update shown in Figure 8a. The arrows represent different tomographic wavepath batches, as explained in the main body of the paper.

To evaluate the performance of ORWI based on PLS-WEM compared to ORWI based on LS-WEM (standard ORWI), for a flat-layered medium shown in Figure 4, we compare the background velocity model update estimated by standard ORWI to that estimated by ORWI equipped with PLS-WEM, both after one cycle. To avoid amplitude fitting in tomography, we use the relative amplitude scaling proposed by Son et al. (2013). With a zero initial reflectivity model, a homogeneous acoustic velocity model of 2000 m/s, a Ricker wavelet with a peak frequency of 10 Hz, surface acquisition, the reflection dataset within the range of 0–15 Hz, a maximum offset of 500 m for migration and a maximum offset of 1000 m for tomography (no cycle-skipping), we run the comparison. After 1 cycle of ORWI, including 1x LS migration and 1x LS tomography, the resultant images and tomograms are shown in Figure 5. As expected, ORWI based on PLS-WEM delivers a superior tomographic update compared to ORWI based on LS-WEM. The superposition of tomographic wavepaths obtained based on PLS-WEM is stronger and more geometrically consistent with the true layers. This enhanced performance is attributed to the improved amplitude preservation and resolution power of PLS-WEM, as shown in Figure 5d.

4 | Optimizing the Tomographic Update in One-Way Reflection Waveform Inversion

In this section, we first examine how well the full-wave consistency condition is met in one-way reflection waveform inversion (ORWI). Next, we suggest three strategies for offset selection

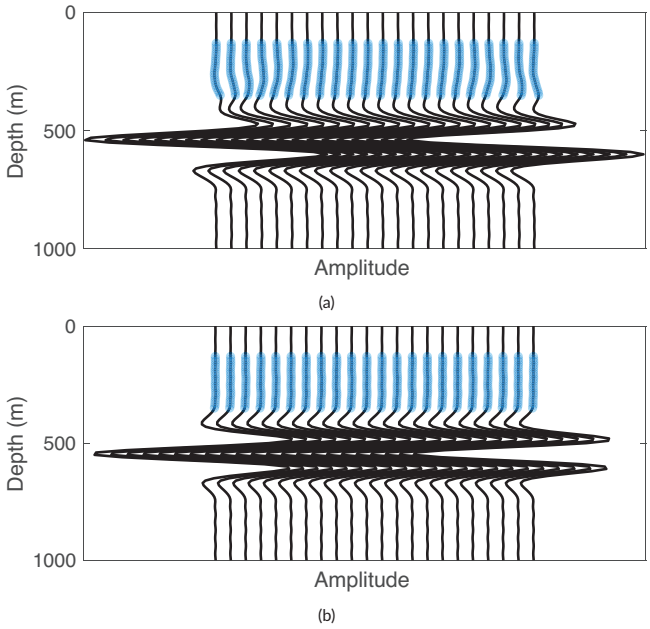

FIGURE 10 | Imaging updates of ORWI for the single-reflector medium (note that on both frames (a) and (b), each wiggle indicates a different lateral location; the lateral locations are ordered from 0 to 5000 m from left to right). (a) Image estimated by the migration mode of ORWI when the data for imaging is cycle-skipped (all migration offsets are included); the image is not focused enough. The lack of focus is evidenced by a phase effect observed in the recovered shape of the reflector and also by non-damped amplitudes preceding the reflector (highlighted in blue). (b) Image estimated by the migration mode of ORWI, where | offsets |> 250 m are muted; the image is focused enough now.

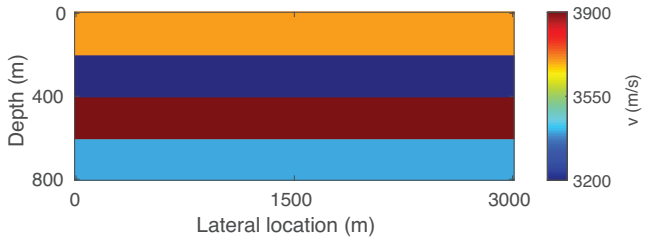

FIGURE 11 | Four-layer medium: True background velocity model.

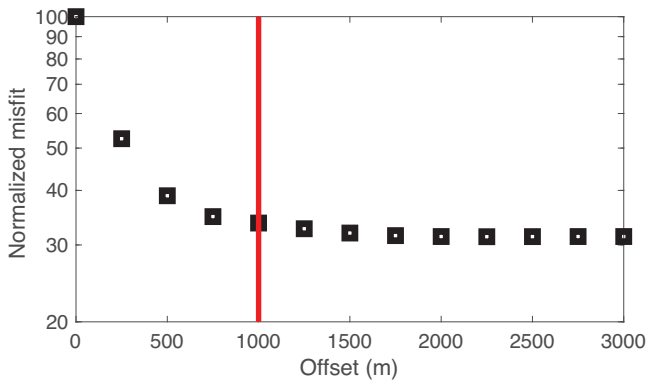

FIGURE 12 | Migration offset analysis to extract the MEMO for the four-layer medium; the red line on the curve denotes the MEMO.

(in both migration and tomography loops) to optimize the tomographic updates in ORWI.

4.1 | Tomographic Update Analysis

A central idea of reflection waveform inversion (RWI) is that the reflectivity model used for the tomographic update allows for fitting the kinematics of the zero-offset observed data (Xu, Wang, Chen, Lambaré, et al. 2012; Xu, Wang, Chen, Zhang, et al. 2012). The assumption is that the velocity errors can be inferred from the time shifts between the observed and modelled traces at larger offsets. While a constant-offset (in particular, zero-offset) migration and demigration can be fully reciprocal in time, amplitude, and phase, this is not necessarily true when a single reflectivity model is computed as the result of a multi-offset migration. Indeed, stacking defocused migrated images from multiple offsets and then demigrating the result into modelled data will create mismatches with the observed data (even if quantitative). Figure 6 shows an interesting illustration of the phenomenon. It compares observed and modelled traces obtained through a full-offset quantitative migration and demigration process for a flat reflector medium with a homogeneous overburden. Figure 6a shows the comparison when the homogeneous initial velocity is greater than the true velocity, and Figure 6b shows when it is smaller. We first observe that the traveltime curves in offset are more open for the modelled traces than for the observed ones when the migration velocity is greater than the true velocity – and the opposite holds when the migration velocity is smaller. We also observe significant changes in wavelet shape and amplitude – not only between observed and modelled traces but also between modelled traces generated with greater or smaller migration velocities (see the relative amplitudes of the three lobes of the wavelet). These observations are particularly evident at short offsets and are what we call full-wave inconsistencies. These observations (i.e., changes in traveltime, amplitude and wavelet behaviour) can be quantified using the ray theory and stationary-phase approximation Bleistein and Handelsman (1986), but that lies beyond the scope of the present paper.

To evaluate the impact of full-wave inconsistency in the short-offset data on ORWI, we here display the tomographic update of ORWI for a single-reflector medium after one cycle. The medium consists of a single reflector and a homogeneous overburden with an acoustic velocity of 3000 m/s (Figure 7a). For the initial background velocity model, a homogeneous model with an acoustic velocity of 2700 m/s is used (Figure 7b). For such a medium, the tomographic updates following one cycle of ORWI, including 1x LS migration and 1x LS tomography, in four different data scenarios are displayed in Figure 8. The data scenarios are listed in Table 1. Note that in the table, offsets with absolute values smaller than 1000 m are counted as uncycle-skipped.

Scenario 1 evaluates how the use of the full-offset data range in both migration and tomography affects the ORWI background velocity update. As evident in Figure 8a, associated with Scenario 1, the background velocity update appears to be completely inefficient. While "ideally" a positive homogeneous velocity update everywhere above the reflector position is expected, an inhomogeneous velocity update with strong vertical variations is retrieved. To have a better understanding, the middle-shot

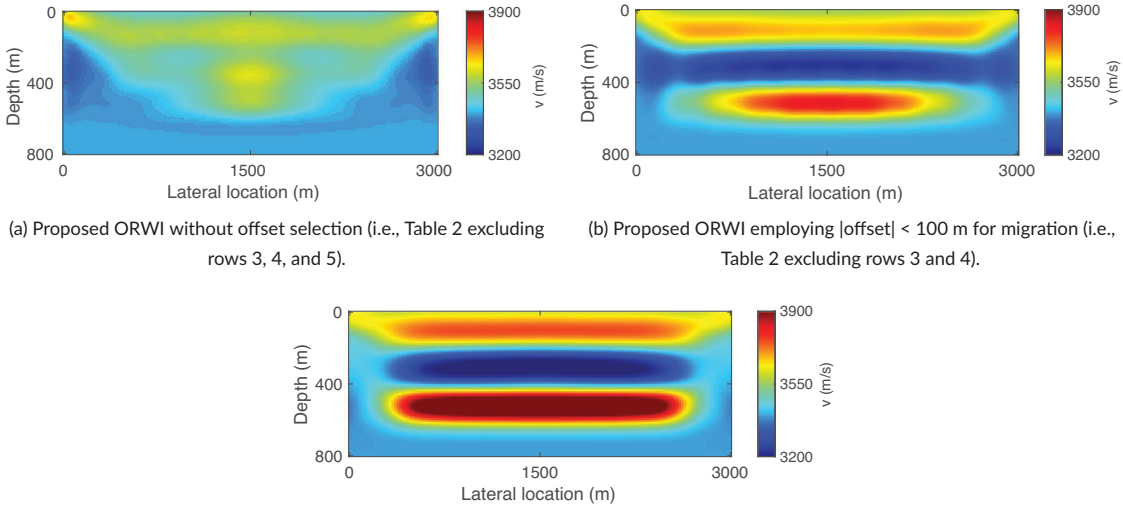

(a) Proposed ORWI without offset selection (i.e., Table 2 excluding rows 3, 4, and 5).

(b) Proposed ORWI employing |offset| < 100 m for migration (i.e., Table 2 excluding rows 3 and 4).

(c) Proposed ORWI (i.e., Table 2 in which MEMO is set to 1000 m based on Figure 12).

FIGURE 13 | Tomographic updates associated with the four-layer medium after 15 cycles. (a) Final background velocity model estimated after 15 cycles of the (a) proposed ORWI without any offset selection, (b) proposed ORWI using short-offset migration and (c) proposed ORWI.

TABLE 1 | Four different data scenarios for retrieving tomographic updates via ORWI.

	Data for imaging	Data for tomography	Imprint of full-wave inconsistency
Scenario 1	Full-offset range	Full-offset range	Present
Scenario 2	Full-offset range	Uncycle-skipped: | offset | <1000 m	Present
Scenario 3	Same range as tomography	Uncycle-skipped: | offset | <1000 m	Present
Scenario 4	Same range as tomography	Uncycle-skipped: | offset | <1000 m	Muted at short offsets

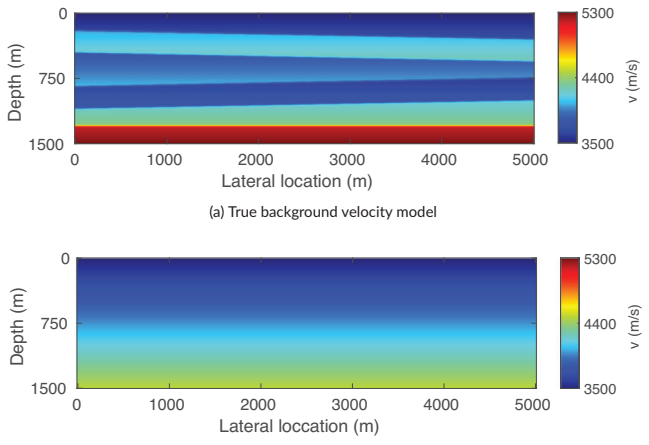

(a) True background velocity model

(b) Initial background velocity model

FIGURE 14 | Two-dipping-layer model (Example 1). (a) True background velocity model. (b) Initial background velocity model.

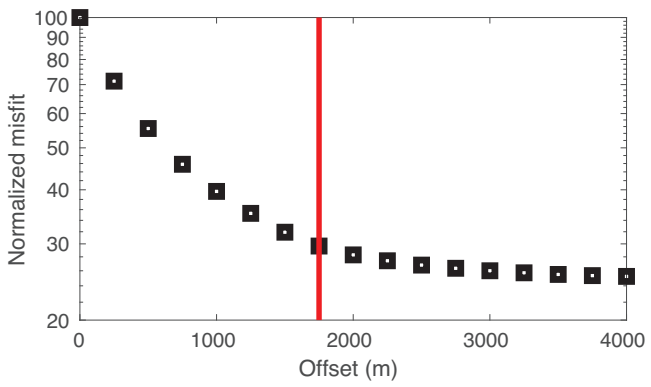

FIGURE 15 | Migration offset analysis to extract the MEMO (Example 1); the red line on the curve denotes the MEMO.

subset of the tomographic update shown in Figure 8a is separately represented in Figure 9. According to Figure 9, the tomographic update can be described as the superposition of three batches of tomographic wavepaths updating against each other: uncycle-skipped mid-to-long-offset tomographic wavepaths, denoted by the grey arrow, increasing the background velocity above the reflector (correct update sign), cycle-skipped long-offset tomographic wavepaths, denoted by the blue arrow, decreasing the background velocity above the reflector (incorrect update sign) and short-offset tomographic wavepaths, denoted by the red arrow, decreasing the background velocity above the reflector (incorrect update sign). These oscillations in the tomographic gradient indicate that the tomographic gradient of ORWI is degraded not only by cycle skipping in long-offset data due to longer propagation in the incorrect velocity but also by full-wave

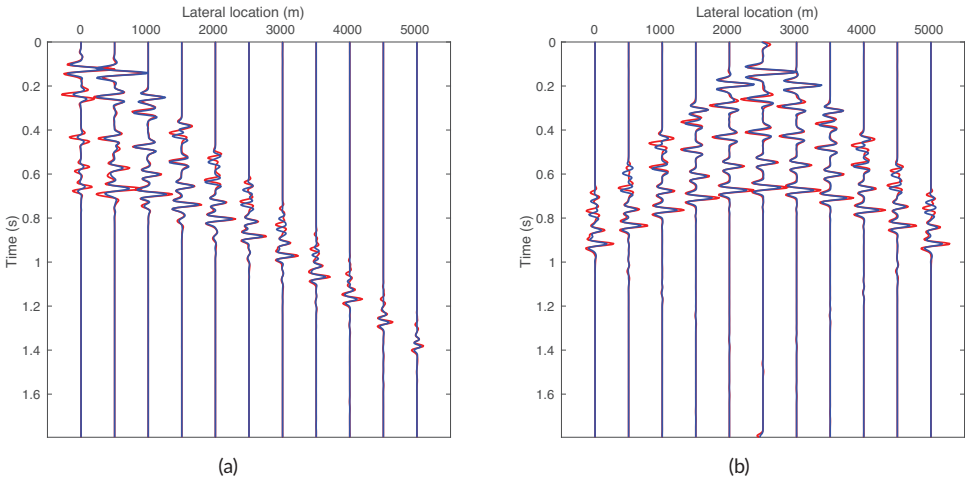

FIGURE 16 | Data fit for the first and middle shots calculated in the true background velocity model, shown in red, and the initial background velocity model, shown in blue (Example 1). (a) First shot gather. (b) Middle shot gather.

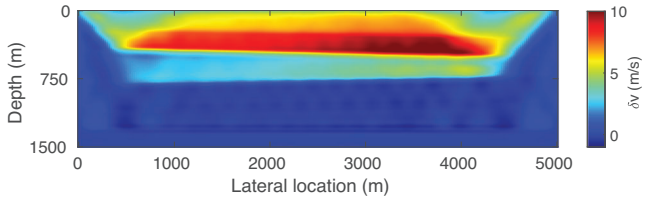

FIGURE 17 | Estimated background velocity model perturbation after 1 cycle of the proposed ORWI (Example 1).

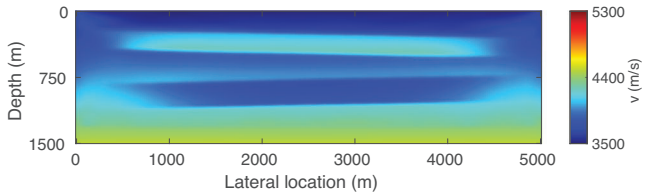

FIGURE 18 | Final estimated background velocity model after 45 cycles of the proposed ORWI (Example 1).

inconsistency in the short-offset data. Note that narrowing the migration offset to short offsets, given the depth of investigation, and increasing the number of LS migration iterations can attenuate the imprint (Provenzano et al. 2023); this last point, however, comes at the price of increased computational cost. Moreover, there might be cases where the short-offset data are either missing or unusable due to technical reasons.

Scenario 2 evaluates the impact of excluding any contribution of the long-offset data to the tomographic gradient to improve the tomographic gradient of ORWI. The background velocity update associated with Scenario 2 is represented in Figure 8b. Clearly, it exhibits weaker vertical variations compared to Scenario 1.

Scenario 3 examines the impact of excluding any contribution of the cycle-skipped long-offset data to the imaging and tomographic gradients to improve the tomographic gradient of ORWI. The background velocity update associated with Scenario 3 is represented in Figure 8c. Compared to the previous scenario, the update exhibits even weaker vertical variations.

Scenario 4 examines the impact of muting short-offset tomographic wavepaths (affected by the full-wave inconsistency in the short-offset data) and excluding contributions of long-offset data to the imaging and tomographic gradients, aiming to improve the tomographic gradient of ORWI. Figure 8d shows the associated background velocity update. As illustrated, Scenario 4 clearly enhances both the magnitude and homogeneity of the background velocity update.

4.2 | Optimal Offset Selection

4.2.1 | Tomography Offset: Short and Mid-to-Long Offsets

Based on the analysis of Scenarios 1–4, we propose muting the tomographic wavepaths affected by full-wave inconsistency in the short-offset data, directly in the residual data gathers and depending on depth. In this paper, we adopt a depth-dependent mute that increases linearly, with a maximum aperture of ±500 m.

4.2.2 | Migration Offset

In the Introduction, it was acknowledged that one approach to mitigate the imprint of full-wave inconsistency in RWI is to use short-offset data for migration. Figure 10a shows the stacked image estimated by the migration mode of standard ORWI for the single-reflector medium (Figure 7) when all migration offsets are included. As can be observed, due to the velocity error and its resultant defocusing, the vertical reflectivity profile is affected in phase and amplitude. Such an effect will definitely affect modelled waveforms in the tomography loop, degrading the full-wave consistency between the short-offset modelled and observed data for tomography. To minimize such error leakage from the migration loop to the tomography loop, a focused image is required. The focused image may be obtained by either improving the background velocity model or removing the non-

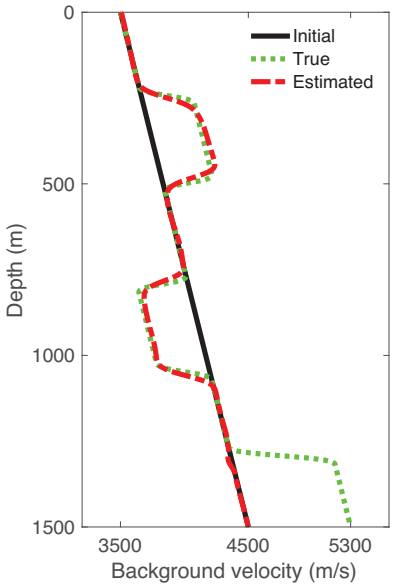

(a) Two-dipping-layer model at the lateral location of 2500 m (Example 1)

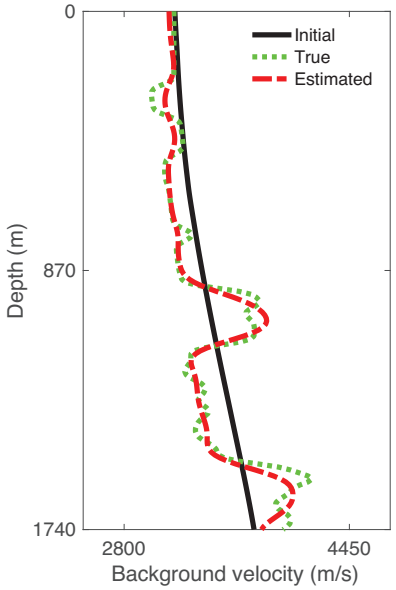

(b) Flat section of the Marmousi model at the lateral location of 3000 m (Example 2)

FIGURE 19 | Vertical background velocity profiles. A vertical profile of the final estimated background velocity model ~~in~~ already shown in (a) Figure 18 at the lateral location of 2500 m and (b) Figure 24 at the lateral location of 3000 m.

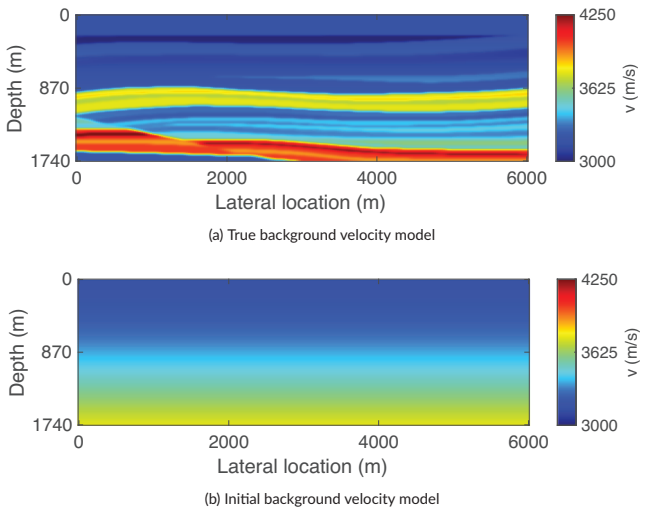

FIGURE 20 | Flat section of the Marmousi model (Example 2). (a) True background velocity model. (b) Initial background velocity model.

focused contributions to the imaging gradient. Since a better velocity model is what ORWI aims to achieve, the second option is the only way forward. However, we have already shown that excluding contributions from long-offset data in imaging though necessary but not sufficient for retrieving an optimal tomographic update (Figure 8: Scenario 3).

As a result, short-offset or even near-zero offset migration has become a widely accepted and effective approach in the RWI community. Figure 10b displays how muting the traces with offsets of absolute values greater than 250 m results in a focused stacked image compared to the original stacked image shown in Figure 10a.

Limiting migration offsets – if it gives a fair match of wavelet shape and amplitude at zero and short offsets – can significantly reduce full-wave inconsistencies in the short-offset data and the need for muting them in tomography. However, stacked images from short- or near-zero offset data may suffer from a low signal-to-noise ratio (SNR) and sub-optimal illumination. While this can be resolved through LS iterations, it increases the computational cost. Extending the migration offset is another way to address the SNR issue, although it compromises reflector focusing, as discussed (Figure 10). Despite this trade-off, extending the migration offset may be justified, as we already mute the short-offset residual waveforms for tomography, where reflector defocusing would cause the most significant damage. The most significant damage occurs at short offsets because, at those offsets, velocity-related errors are largely compensated by depth changes thereby limiting their impact on traveltimes while waveforms remain affected by reflectivity-related errors. Therefore, we suggest extending the migration offset. We extend the migration offset to the point where the misfit function computed based on the full-offset range no longer significantly decreases. At this offset, the amplitude fit does not get any better as the image is mapped by more and more out-of-phase data due to velocity errors. We refer to this as the maximum effective migration offset (MEMO). The MEMO may vary depending on the migration velocity, acquisition geometry and frequency content, and averagely sits somewhere between the near-zero offsets and the maximum uncycle-skipped offset in the data. To set the MEMO, we follow the pseudo-code presented in Algorithm 2 as a pre-processing/QC (quality control) step before running ORWI, which calculates the misfit function value associated with different ranges of offsets (e.g., intervals of 250

ALGORITHM 2 | Migration offset analysis pseudo-code

```
for h ← 0 to max (offset) do
    image← 1x LS migration with h
    p⁻_mod (z_0) ← forward modeling with image and background velocity model
    full-offset residual data← p⁻_obs (z_0) − p⁻_mod (z_0)
    store the misfit function value associated with h
```

m) up to the maximum offset available in the acquisition. On the misfit-offset graph, we pick an offset right before the curve starts to become nearly horizontal on a logarithmic scale (see the discussion on the amplitude vs. offset effect).

4.2.3 | Tomography Offset: Cycle-Skipped Long Offsets

In every seismic waveform-fitting operation, cycle skipping occurs when the initial velocity model is not kinematically accurate enough in order to model the seismic waveforms with less than half a cycle time shift with respect to the observed waveforms in each iteration, leading to a local minimum situation in the corresponding minimization problem (Virieux and Operto 2009). Earlier, we elaborated on the damaging effect of the cycle-skipped long-offset data on tomograms. This section presents a data-selection algorithm to minimize such a damaging effect. While employing an L2-norm waveform-based misfit function in ORWI, we develop an automated algorithm to recognize and exclude the cycle-skipped long-offset reflection data in each tomography loop based on the same idea suggested by van Leeuwen and Mulder (2010).

A given pair of modelled and observed seismic traces in the time domain is called cycle-skipped if their corresponding maximum correlation lag is greater than a reference lag, which is defined based on the dominant period of the observed trace. Based on this, we base our time-domain data-selection algorithm on the cross-correlation of the given traces within a sliding window (local cross-correlation), protected by a global cross-correlation of the given traces beforehand (Algorithm 3). The global cross-correlation serves as a kind of guard to keep the chain of the subsequent local cross-correlations away from facing the irregularities in the modelled waveform before forming maturely. Otherwise, the outputs of the local cross-correlations would not be accurate enough.

In Algorithm 3, for each source location, we run two loops independently (indicated by the counter 'm'), one starting from the receiver index meeting the apex point of the shot gather and increasing, and one starting from the same index but decreasing. In each of these two loops, for each index, we perform global cross-correlation between the modelled and measured traces from the first-break time sample to the last time sample, to calculate the average time delay between the two signals. If the calculated time delay is less than a pre-defined reference time delay (reference lag), then we divide the signals into windows and perform cross-correlation for each window, until a time delay greater than the reference lag is found. If the time delay is greater than the reference lag, we exit the 'for' loop and move on to the next source location. The time delays calculated during each iteration are stored in a time table. As a result, for a given shot gather, the reflection data aperture is not allowed to be extended from the apex point towards the positive/negative offsets unless it satisfies the relevant global cross-correlation as well as the local cross-correlations to the last window.

5 | Proposed One-Way Reflection Waveform Inversion Algorithm

In an effort to resolve the limitations inherent to conventional reflection waveform inversion, as mentioned earlier and listed in the following, we propose our one-way reflection waveform inversion (ORWI) algorithm based on all of the analyses and discussions that we carried out so far. Our proposed ORWI algorithm incorporates the introduced cost-friendly preconditioned least-squares wave equation migration algorithm to retrieve high-resolution amplitude-preserved reflectors, thereby overcoming the challenge of low-resolution seismic images with unpreserved amplitudes in conventional reflection waveform inversion. Muting short-offset residual waveforms in the tomography loop is an additional aspect of our proposal that minimizes the impact of full-wave inconsistency at short offsets. Leveraging these data mute, we advocate extending the migration offset beyond short offsets by calculating the maximum effective migration offset (MEMO) to address limitations in reflection tomography linked to suboptimal low signal-to-noise ratio) and illumination of reflectors. Furthermore, we propose a data-selection algorithm to exclude the negative impact of cycle-skipped long-offset data. The general features of our proposed ORWI algorithm are summarized in Table 2.

It would now be insightful to compare our proposal (Table 2) to when it uses full-offset range for both migration and tomography (no offset selection), and to when it uses short offsets for migration and full offsets for tomography (the common offset selection practice in reflection waveform inversion). To make the comparison, we use a four-layer medium (Figure 11a), with the initial background velocity model being a homogeneous model of 3500 m/s.

Figure 12 displays the resulting graph following Algorithm 2 for the MEMO calculation, considering the initial background velocity model and the full frequency band. Based on the graph, the MEMO is chosen to be 1000 m. After 15 cycles, each including 1x LS migration and 1x LS tomography, Figure 13 exhibits the resultant tomograms.

As observed, while our proposed ORWI accurately estimates the background velocity model of the four-layer medium from

ALGORITHM 3 | Uncycle-skipped data extraction pseudo-code

```
// D_obs and D_mod are 3D matrices representing the observed and modeled data (full-shot).
// n_t × n_g × n_s is the size of D_obs.
// n_t is the total number of time samples.
// n_g and n_s are the total number of receivers and the total number of shots.
// ℓ_w and ℓ_r are the correlation-window length and reference lag.
// ω_c is the current maximum frequency in D.
// ω_m is the peak frequency of the seismic wavelet.
// win_c is the current correlation window.
function CycleSkippingCheck(D_obs, D_mod, n_g, n_s, n_t, ℓ_w, ℓ_r, ω_c, ω_m)
    TIMETABLE ← a matrix of ones of size: n_g × n_s
    for ishot ← 1 to n_s do
        φ ← determine the anchor offset index in the current shot gather
        ι ← φ
        κ ← φ − 1
        for m ← [1, 2] do
            flag ← true
            while (m = 1 and flag = true and ι ≤ n_g) or (m = 2 and flag = true and κ ≤ 1) do
                d_obs, n_obs ← current observed trace and the associated first-break sample
                d_mod ← current modeled trace
                if ω_c > ω_m then
                    d_obs ← d_obs[n_obs : n_t]
                    d_mod ← d_mod[n_obs : n_t]
                else
                    d_obs ← d_obs[1 : n_t]
                    d_mod ← d_mod[1 : n_t]
                calculate cross-correlation between d_obs and d_mod
                if max correlation lag < ℓ_r then
                    win ← [1 : ℓ_w : n_t]
                    b ← length(win)
                    for τ ← 1 to b do
                        win_c ← [1 : win(τ + 1)]
                        calculate cross-correlation between d_obs and d_mod in win_c
                        if max correlation lag < ℓ_r then
                            if τ = b then
                                tmp ← n_t
                            else
                                tmp ← n_obs + win_c(end)
                            if m = 1 then
                                TIMETABLE[ι, ishot] ← tmp
                            else
                                TIMETABLE[κ, ishot] ← tmp
                        else
                            flag ← false
                            break
                else
                    flag ← false
                if m = 1 then
                    ι = ι + 1
                else
                    κ = κ − 1
    return TIMETABLE
```

reflections within 15 cycles (Figure 13c), the two other approaches do not retrieve the layers as effectively as our proposal within the same number of cycles (Figure 13a,b). Although the tomogram estimated using the common offset selection practice (Figure 13b) is a much better estimation than the one obtained with no offset selection (Figure 13a), our proposed approach appears to converge faster. Note that moving closer to zero-offset data for migration and increasing the number of LS iterations can improve the tomogram estimated using the common offset selection practice – though at an increased cost, as noted earlier. This examination shows that the offset selection strategies in our proposed ORWI effectively refine the input data for migration and tomography, reaching the optimal solution in fewer cycles.

6 | Numerical Examples

In this section, we apply our proposed one-way reflection waveform inversion (ORWI) algorithm to three synthetic cases. In all cases, we refine velocity model updates in each cycle using a Gaussian smoothing operator with a standard deviation of 3 (gridpoints).

6.1 | Example 1: Two-Dipping-Layer Model

First, we apply our proposed ORWI algorithm on a two-dipping-layer model, where two dipping layers are placed in a linear

TABLE 2 | General features of our proposed ORWI.

		Proposed ORWI
1	Each cycle	LS migration and LS tomography
2	Migration technology	PLS-WEM
3	Migration offset	| offset | < MEMO based on Algorithm 2
4	Tomography offset	Mid to long
5	Cycle skipping in tomography	Algorithm 3

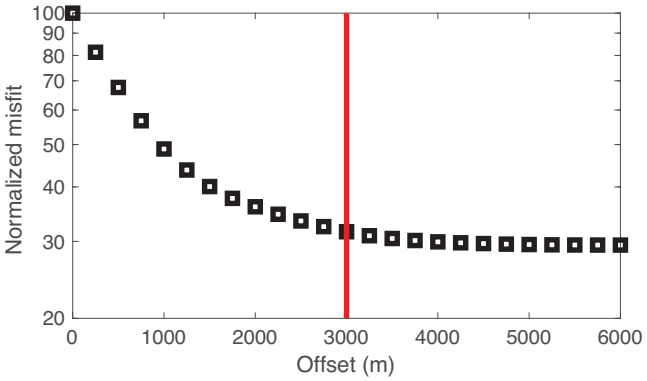

FIGURE 21 | Migration offset analysis to extract the MEMO (Example 2); the red line on the curve denotes the MEMO.

background velocity model (following Warner et al. 2018). Figure 14a and 14b show the true and initial background velocity models, respectively. The model is 5 km in width and 1.5 km in depth and is discretized by 251 × 301 gridpoints with a horizontal grid interval of 20 m and a vertical grid interval of 5 m. As shown, the main task here is to reconstruct the missing layers from the initial background velocity model. The observed dataset, containing only primary reflections, is modelled via PWMod and acquired using 51 surface shots every 100 m and 251 fixed receivers every 20 m. A Ricker wavelet with a peak frequency of 20 Hz is employed as the source function. The maximum available offset in the acquisition is limited to 4000 m. We record the reflection dataset for 1.8 s.

Figure 15 illustrates the migration offset analysis output graph, considering the initial background velocity model and the full frequency band, for this example. According to the misfit-offset graph, we choose the MEMO to be 1750 m (fixed). For tomography, we use offsets larger than 500 m, and any contribution from the cycle-skipped long-offset data into the tomographic gradient is excluded via Algorithm 3 in each cycle. As we progress and update the background velocity, additional offsets become relevant in tomography since they are not cycle-skipped anymore. This continues until all offsets are included. Figure 16 shows the data fit prior to inversion, where cycle skipping is obvious in the dataset.

We invert the full-frequency band 0–60 Hz simultaneously (no multi-scaling strategy) in 45 cycles, each including 1x LS migration and 1x LS tomography. Figure 17 shows the estimated background velocity model perturbation after 1 cycle. As seen, the reconstructed background velocity perturbation accurately represents the true update direction from the very first cycle. Figure 18 shows the final background velocity model estimated after 45 cycles. The result shows a remarkable accuracy in recovering the missing dipping layers in the background velocity. This recovery comes with a high level of vertical resolution. Note that the finite lateral extent of the estimated layers is due to the finite extent of the acquisition. Also, note that we cannot update the deepest layer in the model, below 1300 m, using reflection tomography, as expected. One profile of the final estimated background velocity model is shown in Figure 19a. This profile once more illustrates the effective vertical illumination via our proposed ORWI algorithm.

6.2 | Example 2: Flat Section of the Marmousi Model

Next, we verify our proposed ORWI algorithm with a selected part of the Marmousi model that is almost flat. Figure 20a shows the true background velocity model, which is 6 km in width and 1.74 km in depth. The model is discretized by 251 × 175 gridpoints with a horizontal grid interval of 30 m and a vertical grid interval of 10 m. To construct the initial background velocity model, after smoothing out the true background velocity model using a two-dimensional (2D) Gaussian filter with a standard deviation of 50 (gridpoint), we selected a single vertical profile to construct the initial one-dimensional model. Figure 20b shows the initial background velocity model. Forty-one surface shots are used for acquisition, with a shot spacing of 150 m. There exist 251 fixed receivers distributed on the surface every 10 m. The recording time is 2.2 s. The maximum available offset is limited to 4000 m. Using a Ricker wavelet with a peak frequency of 15 Hz as the source function, the observed reflection dataset, containing only primaries, is generated by PWMod.

Figure 21 displays the migration offset analysis output graph, considering the initial background velocity model and the full frequency band. Based on the misfit-offset graph, the MEMO is fixed at 3000 m. Comparing the MEMO with the maximum available offset in the acquisition, we can infer that the cycle skipping is not that severe in this example. For tomography, offsets larger than 500 m are employed, and the cycle-skipped long-offset data contribution to the tomographic gradient is excluded in each cycle by Algorithm 3. As we advance in cycles and update the background velocity, more and more offsets contribute to tomography because they are no longer cycle-skipped. This process goes on until all offsets are addressed. Figure 22 demonstrates the data fit in the first- and middle-shot gathers prior to inversion, confirming the minimum cycle skipping in the dataset.

We invert the full-frequency band 2–45 Hz at once (no multi-scaling strategy). We perform 150 cycles of the proposed ORWI, each consisting of 1x LS migration and 1x LS tomography. Figure 23a,b displays the cumulative background velocity model perturbation estimated after 1, 50 and 150 cycles. As seen, the recovery of the background velocity model begins with large-scale events and develops towards tiny events. One profile of the

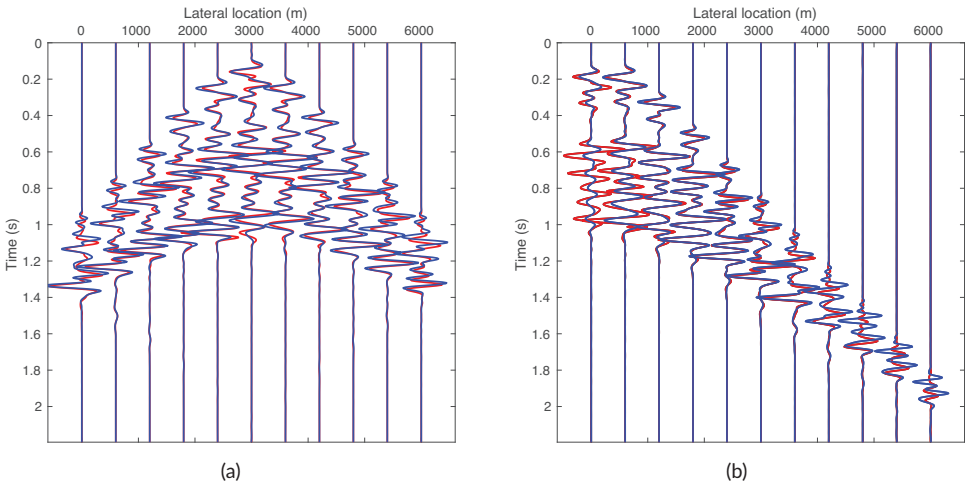

FIGURE 22 | Data fit for the first and middle shots calculated in the true background velocity model, shown in red, and the initial background velocity model, shown in blue (Example 2). (a) First shot gather. (b) Middle shot gather.

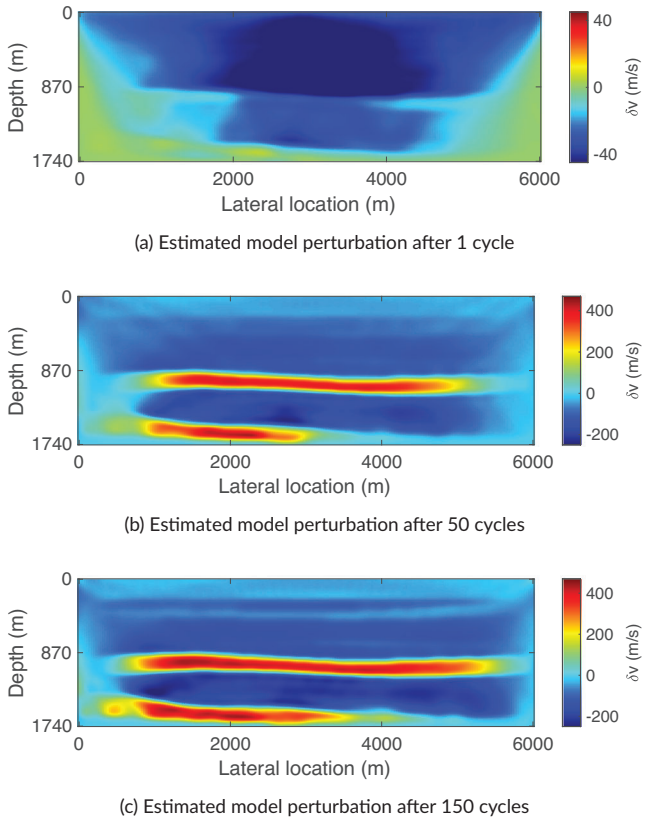

FIGURE 23 | Estimated background velocity model perturbations (Example 2). (a) Estimated background velocity model perturbation after 1 cycle. (b) Cumulative estimated background velocity model perturbation after 50 cycles. (c) Cumulative estimated background velocity model perturbation after 150 cycles.

final estimated background velocity model is also displayed in Figure 19b, revealing a good vertical resolution. Figure 24 shows the final background velocity model estimated after 150 cycles of the proposed ORWI, confirming the effectiveness of the proposal.

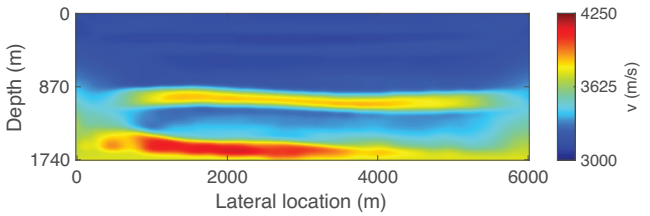

FIGURE 24 | Final estimated background velocity model after 150 cycles of the proposed ORWI (Example 2).

6.3 | Example 3: Faulted Section of the Marmousi Model

Finally, we validate our proposed ORWI algorithm using the faulted section of the Marmousi model (marine scenario). The true background velocity model, illustrated in Figure 25a, spans almost 7 km in width and 2.5 km in depth. This model is discretized into 296 × 104 gridpoints, with a horizontal grid interval of 25 m and a vertical grid interval of 25 m.

To create the initial background velocity model, we apply a 2D Gaussian filter with a standard deviation of 20 (gridpoint) to construct the true background velocity model. The resulting initial background velocity model with a water layer on top is depicted in Figure 25b. For acquisition, 31 surface shots are used on the surface (the shots are spaced either 250 m apart or 225 m apart), and 296 fixed receivers are distributed on the surface at 25 m intervals. The recording time is 4.092 s, and the maximum available offset is limited to 4000 m. Using a Ricker wavelet with a peak frequency of 10 Hz as the source function, we generate the observed reflection dataset, only primaries, through PWMod.

Figure 26 illustrates the output of migration offset analysis, considering the initial background velocity model and the full frequency band, through the misfit-offset graph. The MEMO is set at 2000 m based on the misfit-offset graph. In the tomography process, offsets exceeding 500 m are employed, and the contribution from the cycle-skipped long-offset to the tomographic gradient

TABLE 3 | Frequency strategy employed with Example 3.

	2–3 Hz	2–5 Hz	2–7 Hz	2–14 Hz	2–21 Hz
Total cycle	4	4	4	20	25
LS migration iteration in each cycle	5	5	5	3	2
LS tomography iteration in each cycle	5	5	5	3	2
Image reset to zero after each cycle	Yes	Yes	Yes	Yes	Yes

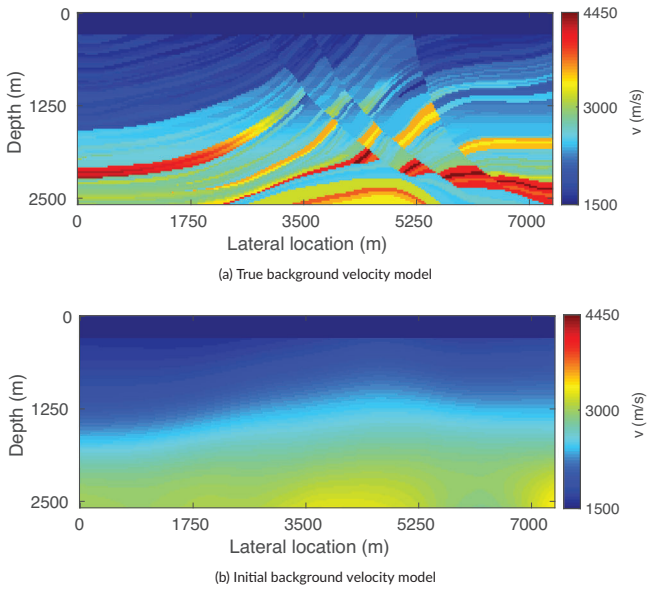

FIGURE 25 | Faulted section of the Marmousi model (Example 3). (a) True background velocity model. (b) Initial background velocity model.

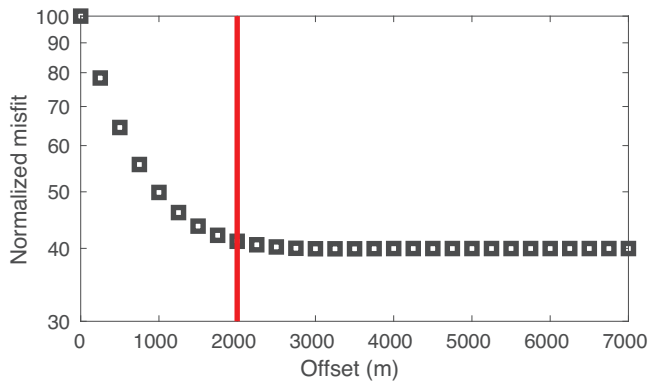

FIGURE 26 | Migration offset analysis to extract the MEMO (Example 3); the red line on the curve denotes the MEMO.

is excluded in each cycle through Algorithm 3. As we progress through cycles and update the background velocity, an increasing number of offsets contribute to tomography since they are no longer cycle-skipped. This process carries on until all offsets have been accounted for.

The inversion here employs a multi-scaling strategy (data are low pass filtered with increasing high cut frequencies), which starts from a low frequency of 2 Hz and gradually increases up to 21 Hz. Table 3 displays the frequency strategy used in the inversion, presenting details on the frequency ranges, the total number of cycles, and the number of iterations for both LS migration and LS tomography within each cycle. Note that the reflectivity model is reset back to zero after each frequency scale. Figure 27a–c shows the estimated background velocity models estimated after the frequency ranges of 2–7 Hz, 2–14 Hz and 2–21 Hz, respectively, and Figure 28a and 28b presents the stacked images mapped using the true, initial estimated and final estimated background velocity models, respectively.

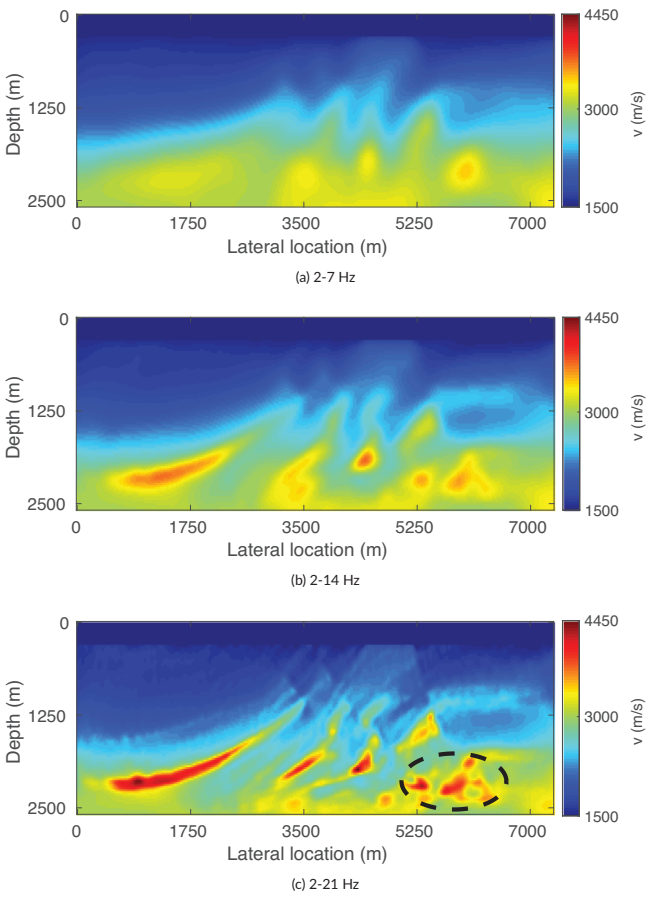

FIGURE 27 | Estimated background velocity models using different frequency ranges (Example 3). (a) Estimated background velocity model with the frequency range of 2–7 Hz. (b) Estimated background velocity model with the frequency range of 2–14 Hz. (c) Estimated background velocity model with the frequency range of 2–21 Hz.

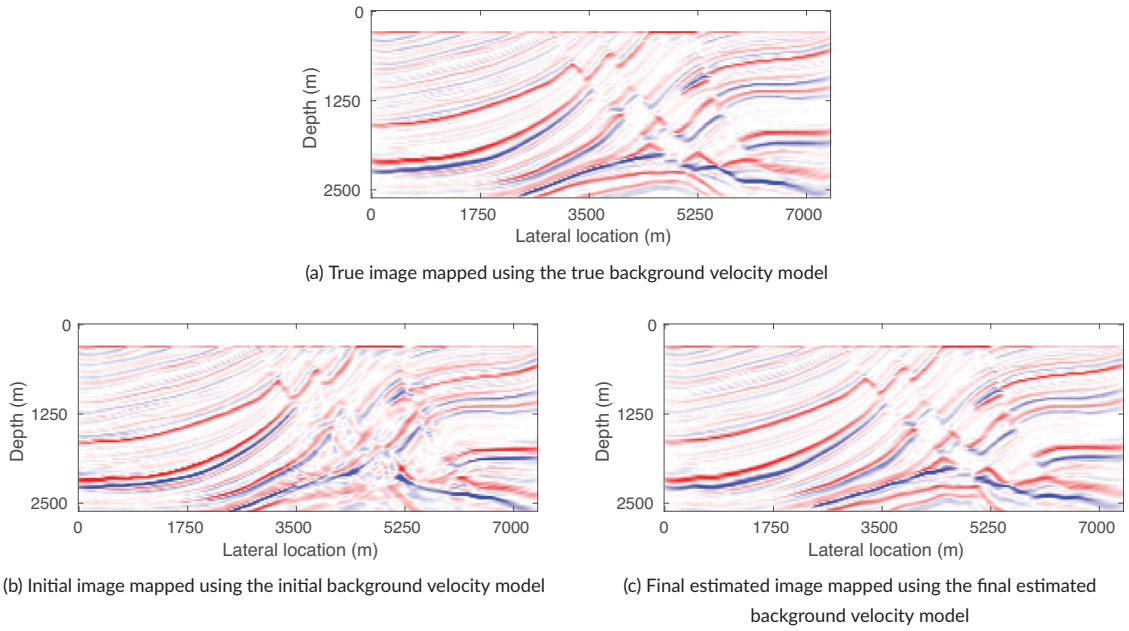

(a) True image mapped using the true background velocity model

(b) Initial image mapped using the initial background velocity model

(c) Final estimated image mapped using the final estimated background velocity model

FIGURE 28 | Estimated images using different background velocity models (Example 3). Estimated images using (a) the true background velocity model, (b) the initial background velocity model and (c) the final estimated background velocity model.

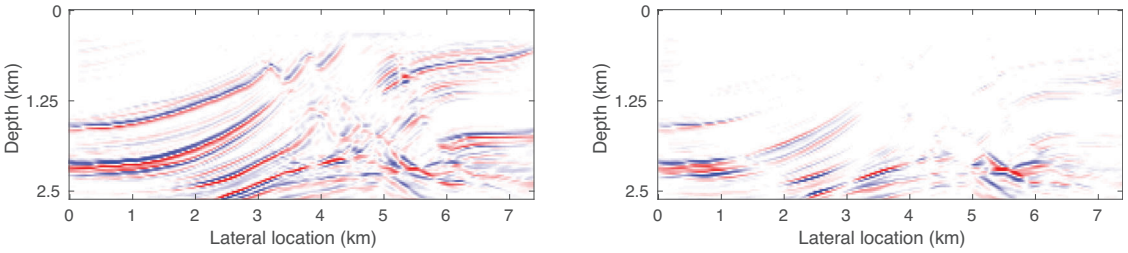

(a) True image - Initial image

(b) True image - Final estimated image

FIGURE 29 | Image difference. (a) Difference between the images mapped by the true and initial background velocity models. (b) Difference between the images mapped by the true and final estimated background velocity models.

As can be seen in Figures 27 and 28, while not flawless, particularly in the deep right of the estimated model marked with a dashed ellipse in Figure 27c, the kinematic properties of the background velocity model during the inversion are improved significantly to incorporate the essential traveltime information for accurate depth migration. For a more precise evaluation of the overall accuracy in estimations, Figure 29 compares the image difference between the true and initial image, as well as the difference between the true and final estimated image.

7 | Discussion

In the field of exploration seismology, full waveform inversion (FWI) has been widely regarded as the ultimate solution for subsurface property reconstruction since its introduction. However, it was later discovered by the FWI community that the reflection-associated tomographic wavepaths in the FWI kernel were too weak to update deep low-wavenumber properties beyond the reach of refractions. In response to this limitation, reflection waveform inversion (RWI) was developed to make full use of the reflection-associated tomographic wavepaths. Despite its potential, RWI has its own limitations, as mentioned earlier. To address these limitations, in the present study, we analysed the current state of RWI in the context of one-way reflection waveform inversion (ORWI).

We acknowledge that our proposed solution to address full-wave inconsistencies in the short-offset data within ORWI is an intermediate step and may not be perfect. It may be viewed as a 'dirty solution' needing further validation and tuning. An alternative promising approach is the one proposed by Liang et al. (2022). Moreover, it should be noted that we have not addressed the issue of reflectivity–velocity coupling, for which solutions have already been proposed – such as working in the pseudo-time domain or explicitly accounting for the coupling when computing the tomographic gradient of RWI (Valensi and Baina 2021).

In this research, we chose not to introduce any model-based regularization to our tomography misfit function. However, we believe that adding a model-based regularization, particularly a structure-oriented type of regularization guided by the reflectivity model (Masaya and Verschuur 2018; Yao, da Silva, and Wu 2019; Provenzano et al. 2023), could positively influence the overall

performance of the tomographic updates. We plan to explore this possibility in future investigations.

The multi-scaling strategy, in the context of RWI, involves inverting the reflection waveforms at multiple scales or frequencies, starting from low frequencies towards higher frequencies. This is done to mitigate the effect of the cycle-skipping issue in the long-offset waveforms in the context of RWI. With Example 3, we showed that a multi-scaling strategy may be beneficial in ORWI wherever the full-band reflection dataset is too complex to be resolved tomographically with the reflection wavepaths all at once. The same is reported in Y. Chen et al. (2020).

Another important aspect for discussion is the amplitude variation with offset (AVO) effect. The ORWI process, given its angle-independent properties, cannot reproduce AVO on the data. Indeed, an angle-independent reflectivity model is insufficient for capturing AVO (Davydenko and Verschuur 2017; Farshad and Chauris 2020). Therefore, we propose to reduce AVO in the data before applying the ORWI methodology, as described in Qu and Verschuur (2021). The examples in this paper were created with the inverse crime approach; that is, we consider the optimum situation where AVO effects do not play a role, such that we can focus on the convergence aspects of ORWI.

There are additional challenges in real data applications. An accurate estimation of the source signal is essential. If there is a mismatch in the source signal, it will bias imaging and tomography results. As the 2D field data still have propagated in a three-dimensional (3D) world, amplitudes have to be corrected (3D to 2D transformation), and out-of-plane effects may not be well addressed by two-dimensional ORWI. Naturally, when ORWI is applied in a full 3D sense to 3D field data, those amplitude and out-of-plane effects will no longer be present. Another challenge with field data is the potential presence of the anisotropy effect. While anisotropy effects can be included in ORWI, updating the anisotropy parameters is not trivial (Alshuhail and Verschuur 2019). The Q-effect in the data can represent another challenge, and this can also be integrated into the ORWI process, as explained by Safari and Verschuur (2023).

Finally, the ORWI method can be extended to the 3D case, where we have wavefields measured along inline and crossline directions. The approximate Hessian matrix for the entire medium will be a 3D block-diagonal matrix, where each block exhibits non-zero elements on and around the main diagonals in three directions, forming a 3D band-diagonal matrix for each virtual data plane, which is still manageable to invert. It will, of course, incur higher computational costs, akin to the entire ORWI method, which is also more expensive in three dimensions.

8 | Conclusion

This paper addressed reflection waveform inversion limitations to recover an improved background velocity model update. To do so, in the context of one-way reflection waveform inversion (ORWI), we replaced the least-squares wave equation migration technology with an efficient preconditioned least-squares wave equation migration technology to retrieve high-resolution reflectors with preserved amplitudes. To mitigate the imprint of full-wave inconsistency in the short-offset data for tomography, we muted short-offset traces in the residual data gathers in the tomographic gradient of ORWI. We also adopted an extended migration offset rather than a short offset to avoid limitations in reflection tomography linked to the suboptimal signal-to-noise ratio and illumination of the reflectivity model. We also proposed a data-selection algorithm to exclude the damaging effect of the cycle-skipped long-offset data from the tomographic gradient of ORWI. The results of three numerical examples demonstrated the effectiveness of the proposed approach in recovering high-fidelity tomograms with good vertical resolution.

Acknowledgements

The authors gratefully acknowledge the contributions of Associate Editor Gilles Lambaré, whose advice and suggestions significantly enhanced this manuscript. The authors also thank the sponsors of the Delphi Consortium for their support.

Data Availability Statement

The data that support the findings of this study are available from the corresponding author upon reasonable request.

References

Abolhassani, S., and D. J. Verschuur. 2024. "Efficient Preconditioned Least-Squares Wave-Equation Migration." *Geophysics* 89: S275–S288.

Alkhalifah, T. 2014. "Scattering-Angle Based Filtering of the Waveform Inversion Gradients." *Geophysical Journal International* 200: 363–373.

Almomin, A., and B. Biondi. 2012. "Tomographic Full Waveform Inversion: Practical and Computationally Feasible Approach." In *SEG Technical Program Expanded Abstracts*: 1–5.

Alshuhail, A. A., and D. J. Verschuur. 2019. "Robust Estimation of Vertical Symmetry Axis Models via Joint Migration Inversion: Including Multiples in Anisotropic Parameter Estimation." *Geophysics* 84: C57–C74.

Assis, C. A., H. Chauris, F. Audebert, and P. Williamson. 2024. "Investigating Hessian-Based Inversion Velocity Analysis." *Geophysics* 89: R169–R186.

Assis, C. A., and J. Schleicher. 2021. "Introduction of the Hessian in Joint Migration Inversion and Improved Recovery of Structural Information Using Image-Based Regularization." *Geophysics* 86: R777–R793.

Audebert, F., and E. Cocher. 2020. "Accounting for the Depth-Velocity Coupling in Reflection Full Waveform Inversion (RFWI)." In *SEG Technical Program Expanded Abstracts*: 3659–3663.

Baina, R., and R. Valensi. 2018. "Borrowing Insight from Travel-Time Reflection Tomography to Solve the Depth Reflectivity-Velocity Coupling Issue of RFWI." In *the 80th EAGE Annual Conference & Exhibition, Workshops*, June 2018, cp–556–00013. European Association of Geoscientists & Engineers.

Berkhout, A. J. 1982. "*Developments in Solid Earth Geophysics*." *Vol.* 14, *Part A, Seismic Migration, Imaging of Acoustic Energy by Wave Field Extrapolation, A: Theoretical Aspects*. Elsevier.

Berkhout, A. J.. 2012. "Combining Full Wavefield Migration and Full Waveform Inversion, A Glance into the Future of Seismic Imaging." *Geophysics* 77: S43–S50.

Berkhout, A. J. 2014a. "Review Paper: an Outlook on the Future Seismic Imaging, Part I: Forward and Reverse Modeling."*Geophysical Prospecting* 62: 911–930.

Berkhout, A. J. 2014b. "Review Paper: an Outlook on the Future Seismic Imaging, Part III: Joint Migration Inversion."*Geophysical Prospecting* 62: 950–971.

Beydoun, W. B., and M. Mendes. 1989. "Elastic Ray-Born l2-Migration/Inversion." *Geophysical Journal International* 97: 151–160.

Bleistein, N., and R. A. Handelsman. 1986. *Asymptotic Expansions of Integrals*. Courier Corporation.

Bozdağ, E., J. Trampert, and J. Tromp. 2011. "Misfit Functions for Full Waveform Inversion Based on Instantaneous Phase and Envelope Measurements." *Geophysical Journal International* 185: 845–870.

Brittan, J., and I. Jones. 2019. "FWI Evolution – From a Monolith to a Toolkit." *The Leading Edge* 38: 179–184.

Bunks, C., F. M. Saleck, S. Zaleski, and G. Chavent. 1995. "Multiscale Seismic Waveform Inversion." *Geophysics* 60: 1457–1473.

Chauris, H., and E. Cocher. 2017. "From Migration to Inversion Velocity Analysis." *Geophysics* 82: S207–S223.

Chauris, H., and E. Cocher. 2018. "Review of Different Expressions for the Extended Born Approximate Inverse Operator." In *the 80th EAGE Annual Conference & Exhibition, Workshops*, cp–556–00032. European Association of Geoscientists & Engineers.

Chauris, H., D. Donno, and H. Calandra. 2012. "Velocity Estimation with the Normalized Integration Method." In *74th EAGE Conference & Exhibition incorporating EUROPEC*, cp–293–00725, Extended abstract. European Association of Geoscientists & Engineers.

Chauris, H., and M. Farshad. 2023. "Seismic Differential Semblance-Oriented Migration Velocity Analysis—Status and the Way Forward." *Geophysics* 88: U81–U100.

Chauris, H., and M. Noble. 2001. "Two-Dimensional Velocity Macro Model Estimation from Seismic Reflection Data by Local Differential Semblance Optimization: Applications to Synthetic and Real Data Sets." *Geophysical Journal International* 144: 14–26.

Chavent, G., F. Clément, and S. Gómez. 1994. "Automatic Determination of Velocities via Migration-Based Traveltime Waveform Inversion: a Synthetic Data Example." In *SEG Technical Program Expanded Abstracts*: 1179–1182.

Chavent, G., and R. E. Plessix. 1999. "An Optimal True-Amplitude Least-Squares Prestack Depth-Migration Operator." *Geophysics* 64: 508–515.

Chen, G.-X., R.-S. Wu, and S.-C. Chen. 2018. "Reflection Multi-Scale Envelope Inversion." *Geophysical Prospecting* 66: 1258–1271.

Chen, Y., Z. Feng, L. Fu, A. AlTheyab, S. Feng, and G. Schuster. 2020. "Multiscale Reflection Phase Inversion With Migration Deconvolution." *Geophysics* 85: R55–R73.

Chi, B., L. Dong, and Y. Liu. 2014. "Full Waveform Inversion Method Using Envelope Objective Function Without Low Frequency Data." *Journal of Applied Geophysics* 109: 36–46.

Chi, B., K. Gao, and L. Huang. 2017. "Least-Squares Reverse Time Migration Guided Full-Waveform Inversion." In *SEG Technical Program Expanded Abstracts*: 1471–1475.

Choi, Y., and T. Alkhalifah. 2013. "Frequency-Domain Waveform Inversion Using the Phase Derivative." *Geophysical Journal International* 195: 1904–1916.

Choi, Y., and T. Alkhalifah. 2014. "Two-Dimensional Unwrapped Phase Inversion with Damping and a Gaussian Filter." In *76th EAGE Conference & Exhibition*, June 2014, Volume 2014: 1–5, Extended Abstracts. European Association of Geoscientists & Engineers.

Choi, Y., T. Alkhalifah, and B. DeVault. 2015. "Application of the Unwrapped Phase Inversion to Land Data without Source Estimation." In *SEG Technical Program Expanded Abstracts*: 1225–1229.

Choi, Y., D.-J. Min, and C. Shin. 2008. "Frequency-Domain Elastic Full Waveform Inversion Using the New Pseudo-Hessian Matrix: Experience of Elastic Marmousi-2 Synthetic Data." *Bulletin of the Seismological Society of America* 98: 2402–2415.

Clément, F. 1991. A Migration-Based Travel-Time Formulation for the Inversion of 2D Seismic Reflection Data. Paper presented at the First International Conference on Mathematical and Numerical Aspects of Wave Propagation Phenomena, Strasbourg, France, April 23–26, 1991.

Davydenko, M., and D. J. Verschuur. 2017. "Full-Wavefield Migration: Using Surface and Internal Multiples in Imaging." *Geophysical Prospecting* 65: 7–21.

de Hoop, M. V., and R. D. van Der Hilst. 2005. "On Sensitivity Kernels for Wave-Equation Transmission Tomography." *Geophysical Journal International* 160: 621–633.

Dong, L., Z. Fan, H. Wang, B. Chi, and Y. Liu. 2018. "Correlation-Based Reflection Waveform Inversion by One-Way Wave Equations." *Geophysical Prospecting* 66: 1503–1520.

Donno, D., H. Chauris, and H. Calandra. 2013. "Estimating the Background Velocity Model With the Normalized Integration Method." In *75th EAGE Conference & Exhibition incorporating SPE EUROPEC* 2013, cp–348–00956, Extended Abstracts. European Association of Geoscientists & Engineers.

Farshad, M., and H. Chauris. 2020. "From Constant to Variable-Density Inverse Extended Born Modeling." *Geophysics* 85: S217–S232.

Fletcher, R. P., D. Nichols, R. Bloor, and R. T. Coates. 2016. "Least-Squares Migration - Data Domain Versus Image Domain Using Point Spread Functions." *The Leading Edge* 35: 157–162.

Gomes, A., and Z. Yang. 2018. "Improving Reflection FWI Reflectivity Using LSRTM in the Curvelet Domain." In *SEG Technical Program Expanded Abstracts*: 1248–1252.

Guitton, A. 2004. "Amplitude and Kinematic Corrections of Migrated Images for Nonunitary Imaging Operators." *Geophysics* 69: 1017–1024.

Guo, Q., and T. Alkhalifah. 2017. "Elastic Reflection-Based Waveform Inversion with A Nonlinear Approach." *Geophysics* 82: R309–R321.

Hassine, A. B., V. Duprat, R. Baina, and D. Brito. 2022. "One-Way WaveForm Inversion (OWI)." In *the 83rd EAGE Annual Conference & Exhibition*, 1–5, Extended Abstracts. *European Association of Geoscientists & Engineers*.

Hou, J., and W. W. Symes. 2015. "An Approximate Inverse to the Extended Born Modeling Operator." *Geophysics* 80: R331–R349.

Hou, J., and W. W. Symes. 2016. "Approximate Gauss-Newton Iteration for Full-Waveform Inversion." In *SEG Technical Program Expanded Abstracts*: 1163–1168.

Hu, J., G. T. Schuster, and P. Valasek. 2001. "Poststack Migration Deconvolution." *Geophysics* 66: 939–952.

Irabor, K., and M. Warner. 2016. "Reflection FWI." In *SEG Technical Program Expanded Abstracts*: 1136–1140.

Jang, U., D.-J. Min, and C. Shin. 2009. "Comparison of Scaling Methods for Waveform Inversion." *Geophysical Prospecting* 57: 49–59.

F Jones, I. 2019. "Tutorial: The Mechanics of Waveform Inversion." *First Break* 37: 31–43.

Kazei, V., E. Tessmer, and T. Alkhalifah. 2016. "Scattering Angle-Based Filtering via Extension in Velocity." In *SEG Technical Program Expanded Abstracts*: 1157–1162.

Kiyashchenko, D., R.-E. Plessix, B. Kashtan, and V. Troyan. 2007. "A Modified Imaging Principle for True-Amplitude Wave-Equation Migration." *Geophysical Journal International* 168: 1093–1104.

Lecomte, I. 2008. "A Ray-Based Approach: Resolution and Illumination Analyses in PSDM." *The Leading Edge* 27: 650–663.

Li, Y., Q. Guo, Z. Li, and T. Alkhalifah. 2019. "Elastic Reflection Waveform Inversion with Variable Density." *Geophysics* 84: R553–R567.

Lian, S., S. Yuan, G. Wang, T. Liu, Y. Liu, and S. Wang. 2018. "Enhancing Low-Wavenumber Components of Full-Waveform Inversion Using an Improved Wavefield Decomposition Method in the Time-Space Domain." *Journal of Applied Geophysics* 157: 10–22.

Liang, H., H. Zhang, and H. Liu. 2022. "Analysis of the Impact of Demigration on Traveltime-Based Reflection Full-Waveform Inversion." In *SEG Technical Program Expanded Abstracts*: 1002–1006.

Lines, L., and S. Treitel. 1984. "A Review of Least-Squares Inversion and Its Application to Geophysical Problems." *Geophysical Prospecting* 32: 159–186.

Liu, F., L. Guash, S. C. Morton., et al. 2012. "3D Time-Domain Full Waveform Inversion of a Valhall OBC Dataset." In *SEG Technical Program Expanded Abstracts*: 1–5.

Liu, F., G. Zhang, S. A. Morton, and J. P. Leveille. 2011. "An Effective Imaging Condition for Reverse-Time Migration Using Wavefield Decomposition." *Geophysics* 76: S29–S39.

Lu, S., F. Liu, N. Chemingui, A. Valenciano, and A. Long. 2018. "Least-Squares Full-Wavefield Migration." *The Leading Edge* 37: 46–51.

Luo, Y., Y. Ma, Y. Wu, H. Liu, and L. Cao. 2016. "Full-Traveltime Inversion." *Geophysics* 81: R261–R274.

Luo, Y., and G. T. Schuster. 1991. "Wave-Equation Traveltime Inversion." *Geophysics* 56: 645–653.

Ma, Y., and D. Hale. 2013. "Wave-Equation Reflection Traveltime Inversion With Dynamic Warping and Full-Waveform Inversion." *Geophysics* 78: R223–R233.

Masaya, S., and D. Verschuur. 2018. "Iterative Reflectivity-Constrained Velocity Estimation for Seismic Imaging." *Geophysical Journal International* 214: 1–13.

Mora, P. 1989. "Inversion = Migration + Tomography." *Geophysics* 54: 1575–1586.

Métivier, L., R. Brossier, Q. Mérigot, E. Oudet, and J. Virieux. 2016. "Measuring the Misfit Between Seismograms Using an Optimal Transport Distance: Application to Full Waveform Inversion." *Geophysical Journal International* 205: 345–377.

Métivier, L., R. Brossier, J. Virieux, and S. Operto. 2013. "Full Waveform Inversion and the Truncated Newton Method." *SIAM Journal on Scientific Computing* 35: B401–B437.

Oh, J.-W., and D.-J. Min. 2013. "Weighting Technique Using Backpropagated Wavefields Incited by Deconvolved Residuals for Frequency-Domain Elastic Full Waveform Inversion." *Geophysical Journal International* 194: 322–347.

Plessix, R. E., P. Milcik, H. Rynja, A. Stopin, and K. Matson. 2013. "Multiparameter Full Waveform Inversion: Marine and Land Examples." *The Leading Edge* 32: 1030–1038.

Plessix, R. E., and W. A. Mulder. 2004. "Frequency-Domain Finite-Difference Amplitude-Preserving Migration." *Geophysical Journal International* 157: 975–987.

Pratt, R. G., C. Shin, and G. J. Hicks. 1998. "Gauss–Newton and Full Newton Methods In Frequency-Space Seismic Waveform Inversion." *Geophysical Journal International* 133: 341–362.

Provenzano, G., R. Brossier, and L. Métivier. 2023. "Robust and Efficient Waveform-Based Velocity-Model Building by Optimal Transport in the Pseudotime Domain: Methodology." *Geophysics* 88: U49–U70.

Qin, B., and G. Lambaré. 2016. "Joint Inversion of Velocity and Density in Preserved-Amplitude Full-Waveform Inversion." In *SEG Technical Program Expanded Abstracts*: 1325–1330.

Qu, S., Y. van den Brule, and D. J. Verschuur. 2020. "A Stable Scheme of Joint Migration Inversion in the Pseudo-Time Domain." In *the EAGE Annual Conference & Exhibition Online*, 1–5, Extended Abstracts. *European Association of Geoscientists & Engineers*.

Qu, S., and D. Verschuur. 2021. "An Effective Scheme of Pseudo-Time Joint Migration Inversion with an AVO Mitigating Workflow." In *the 82nd EAGE Annual Conference & Exhibition*, 1–5, Extended Abstracts. *European Association of Geoscientists & Engineers*.

Robin, A., R. Valensi, R. Baina, and S. Zhang. 2023. "An Application of the Time Consistent Waveform Inversion (TWIN) Method to a Marine Dataset." In the 84rd EAGE Annual Conference & Exhibition, 1–5, Extended Abstracts. European Association of Geoscientists & Engineers.

Romahn, S., K. A. Innanen, and G. F. Margrave. 2021. "Log-Validated Waveform Inversion of Reflection Seismic Data With Wavelet Phase and Amplitude Updating." *Geophysics* 86: R529–R546.

Safari, M., and J. Verschuur. 2023. "Joint Migration Inversion Including Q Effects: towards Q Estimation." In *the 84th EAGE Annual Conference & Exhibition*, 1–5, Extended Abstracts. *European Association of Geoscientists & Engineers*.

Sava, P., and B. Biondi. 2004. "Wave-Equation Migration Velocity Analysis. I. Theory." *Geophysical Prospecting* 52: 593–606.

Shen, P. 2005. *Wave Equation Migration Velocity Analysis by Differential Semblance Optimization*. Ph.D. thesis, Rice University.

Shen, P., and W. W. Symes. 2008. "Automatic Velocity Analysis via Shot Profile Migration." *Geophysics* 73: VE49–VE59.

Shen, P., W. W. Symes, and C. C. Stolk. 2003. "Differential Semblance Velocity Analysis by Wave-Equation Migration." In *SEG Technical Program Expanded Abstracts*: 2132–2135.

Shin, C., C. S. Jang, and D.-J. Min. 2001. "Improved Amplitude Preservation for Prestack Depth Migration by Inverse Scattering Theory." *Geophysical Prospecting* 49: 592–606.

Son, M., Y. Kim, C. Shin, and D.-J. Min. 2013. "Time Domain Full Waveform Inversion Using a Time-Window and Huber Function Norm." *Journal of Seismic Exploration* 22: 311–338.

Soubaras, R., B. Gratacos, R. Sablon, and J. Lie. 2023. "Fast-Track Simultaneous Velocity and Reflectivity Inversion Using One-Way Modelling: a North Sea Example." In the 84th EAGE Annual Conference & Exhibition, 1–5. *European Association of Geoscientists & Engineers*.

Sun, D., K. Jiao, X. Cheng, and D. Vigh. 2016. "Reflection-Based Waveform Inversion." In *SEG Technical Program Expanded Abstracts*: 1151–1156.

Sun, D., and W. Symes. 2013. Waveform Inversion via Nonlinear Differential Semblance Optimization. Paper presented at the 75th EAGE Conference & Exhibition incorporating SPE EUROPEC, Workshops. European Association of Geoscientists & Engineers.

Sun, Y., E. Verschuur, and S. Qu. 2019. "Research Note: Derivations of Gradients in Angle-Independent Joint Migration Inversion." *Geophysical Prospecting* 67: 572–579.

W Symes, W.. 2008. "Migration Velocity Analysis and Waveform Inversion." *Geophysical Prospecting* 56: 765–790.

Tang, Y., S. Lee, A. Baumstein, and D. Hinkley. 2013. "Tomographically Enhanced Full Wavefield Inversion." In *SEG Technical Program Expanded Abstracts*: 1037–1041.

Tarantola, A. 1984. "Inversion of Seismic Reflection Data in the Acoustic Approximation." *Geophysics* 49: 1259–1266.

ten, Kroode, F,. 2012. "A Wave-Equation-Based Kirchhoff Operator." *Inverse Problems* 28: 115013.

ten Kroode, F. 2014. "A Lie Group Associated to Seismic Velocity Estimation." In *Inverse Problems From Theory to Applications Conference*, 142–146. Institute of Physics Publishing.

Thorbecke, J. W., K. Wapenaar, and G. Swinnen. 2004. "Design of One-Way Wavefield Extrapolation Operators, Using Smooth Functions in Wlsq Optimization." *Geophysics* 69: 1037–1045.

Valenciano, A. A., B. Biondi, and A. Guitton. 2006. "Target-Oriented Wave-Equation Inversion." *Geophysics* 71: A35–A38.

Valensi, R., and R. Baina. 2021. "A Time Consistent Waveform Inversion (TWIN) Method." In the 82nd EAGE Annual Conference & Exhibition, 1–5. Extended Abstracts. *European Association of Geoscientists & Engineers*.

van Leeuwen, T., and W. A. Mulder. 2010. "A Correlation-Based Misfit Criterion for Wave-Equation Traveltime Tomography." *Geophysical Journal International* 182: 1383–1394.

Verschuur, D. J., X. R. Staal, and A. J. Berkhout. 2016. "Joint Migration Inversion: Simultaneous Determination of Velocity Fields and Depth Images Using All Orders of Scattering." *The Leading Edge* 35: 1037–1046.

Vigh, D., D. K. Jiao, X. Cheng, D. Sun, and W. Lewis. 2016. "Earth-Model Building From Shallow to Deep With Full-Waveform Inversion." *The Leading Edge* 35: 1025–1030.

Vigh, D., J. Kapoor, and H. Li. 2011. "Full-Waveform Inversion Application in Different Geological Settings." In *SEG Technical Program Expanded Abstracts*: 2374–2378.

Virieux, J., and S. Operto. 2009. "An Overview of Full-Waveform Inversion in Exploration Geophysics." *Geophysics* 74: WCC1–WCC26.

Wang, F., H. Chauris, D. Donno, and H. Calandra. 2013. "Taking Advantage of Wave Field Decomposition in Full Waveform Inversion." In *75th EAGE Conference & Exhibition incorporating SPE EUROPEC*, cp–348–00960, Extended Abstracts. European Association of Geoscientists & Engineers.

Wang, P., Z. Zhang, Z. Wei, and R. Huang. 2018. "A Demigration-Based Reflection Full-Waveform Inversion Workflow." In *SEG Technical Program Expanded Abstracts*: 1138–1142.

Warner, M., T. Nangoo, A. Umpleby, N. Shah, and G. Yao. 2018. "High-Resolution Reflection FWI." In the 80th EAGE Annual Conference & Exhibition, 1–5, Extended Abstracts. *European Association of Geoscientists & Engineers*.

Wu, R. S., J. Luo, and B. Wu. 2014. "Seismic Envelope Inversion and Modulation Signal Model." *Geophysics* 79: WA13–WA24.

Wu, Z., and T. Alkhalifah. 2015. "Simultaneous Inversion of the Background Velocity and the Perturbation in Full-Waveform Inversion." *Geophysics* 80: R317–R329.

Wu, Z., and T. Alkhalifah. 2017. "Efficient Scattering-Angle Enrichment for a Nonlinear Inversion of the Background and Perturbations Components of a Velocity Model." *Geophysical Journal International* 210: 1981–1992.

Xie, X.-B. 2015. "An Angle-Domain Wavenumber Filter for Multi-Scale Full-Waveform Inversion." In *SEG Technical Program Expanded Abstracts*. Technical Program Expanded Abstracts: 1132–1137.

Xu, S., D. Wang, F. Chen, G. Lambaré, and Y. Zhang. 2012. "Inversion on Reflected Seismic Wave." In *SEG Technical Program Expanded Abstracts*: 1–7.

Xu, S., D. Wang, F. Chen, Y. Zhang, and G. Lambaré. 2012. "Full Waveform Inversion for Reflected Seismic Data." In *the 74th EAGE Annual Conference & Exhibition*, cp–293–00729, Extended abstract. European Association of Geoscientists & Engineers.

Yang, Y., and B. Engquist. 2018. "Analysis of Optimal Transport and Related Misfit Functions in Full-Waveform Inversion." *Geophysics* 83: A7–A12.

Yao, G., N. V. da Silva, V. Kazei, D. Wu, and C. Yang. 2019. "Extraction of the Tomography Mode With Nonstationary Smoothing for Full-Waveform Inversion." *Geophysics* 84: R527–R537.

Yao, G., N. V. da Silva, M. Warner, and T. Kalinicheva. 2018. "Separation of Migration and Tomography Modes of Full-Waveform Inversion in the Plane Wave Domain." *Journal of Geophysical Research: Solid Earth* 123: 1486–1501.

Yao, G., N. V. da Silva, and D. Wu. 2019. "Reflection-Waveform Inversion Regularized with Structure-Oriented Smoothing Shaping." *Pure and Applied Geophysics* 176: 5315–5335.

Yao, G., D. Wu, and S. Wang. 2020. "A Review on Reflection-Waveform Inversion." *Petroleum Science* 17: 334–351.

Yu, J., J. Hu, G. T. Schuster, and R. Estill. 2006. "Prestack Migration Deconvolution." *Geophysics* 71: S53–S62.

Zhang, Y., S. Xu, N. Bleistein, and G. Zhang. 2007. "True-Amplitude, Angle-Domain, Common-Image Gathers From One-Way Wave-Equation Migrations." *Geophysics* 72: S49–S58.

Zhou, H., L. Amundsen, and G. Zhang. 2012. "Fundamental Issues in Full Waveform Inversion." In *SEG Technical Program Expanded Abstracts*: 1–5.

Zhou, W., R. Brossier, S. Operto, and J. Virieux. 2015. "Full Waveform Inversion of Diving Waves for Velocity Model Building With Impedance Inversion Based on Scale Separation." *Geophysical Journal International* 202: 1535–1554.